A Parameterization for the Triggering of Landscape Generated Moist Convection

by

Barry H. Lynn[1,2], Wei-Kuo Tao[2], and Frank Abramopoulos[3]

[1]*Columbia University Center for Climate System Research*
New York, New York

[2]*NASA Goddard Space Flight Center*
Mesoscale Atmospheric Processes Branch
Greenbelt, Maryland

[3]*Science Systems and Applications Inc.*
NASA Goddard Institute for Space Studies
New York, New York

J. of Atmos. Sci.

(Submitted November 6, 1998)

Corresponding author address: Dr. Barry Lynn, Mesoscale Atmospheric Processes Branch, Code 912, NASA/GSFC, Greenbelt, MD 20771
email: lynn@agnes.gsfc.nasa.gov

Abstract

A set of relatively high resolution three-dimensional (3D) simulations were produced to investigate the triggering of moist convection by landscape generated mesoscale circulations. The *local* accumulated rainfall varied monotonically (linearly) with the size of individual landscape patches, demonstrating the need to develop a trigger function that is sensitive to the size of individual patches. A new triggering function that includes the effect of landscape generated mesoscale circulations over patches of different sizes consists of a parcel's perturbation in vertical velocity (w_o), temperature (θ_o), and moisture (q_o). Each variable in the triggering function was also sensitive to soil moisture gradients, atmospheric initial conditions, and moist processes. The parcel's vertical velocity, temperature, and moisture perturbation were partitioned into mesoscale and turbulent components. Budget equations were derived for θ_o and q_o. Of many terms in this set of budget equations, the turbulent, vertical flux of the mesoscale temperature and moisture contributed most to the triggering of moist convection through the impact of these fluxes on the parcel's temperature and moisture profile. These fluxes needed to be parameterized to obtain θ_o and q_o. The mesoscale vertical velocity also affected the profile of w_o. We used similarity theory to parameterize these fluxes, as well as the parcel's mesoscale vertical velocity.

1 Introduction

Analysis of observational data and simulation results obtained over heterogeneous land surfaces can reveal both turbulent and mesoscale processes. For example, turbulent eddies can be superimposed upon mesoscale circulations that are generated by landscape discontinuities (Mahrt, 1987, Balling, 1988, Segal *et al.* 1989; Smith *et al.*, 1992; Mahrt *et al.*, 1994; Chen and Avissar, 1994; Pielke *et al.*, 1997; Vidale *et al.*, 1997; Lynn *et al.*, 1998). These mesoscale circulations generate sea-breeze-like fronts, which can be associated with relatively large vertical velocity, temperature, and moisture perturbations. Studies with numerical models and some observational results have shown that these sea-breeze-like fronts produce both shallow and deep convection (*e.g.*, Chen and Avissar, 1994; Cutrim *et al.* 1995; Avissar and Liu, 1996; Lynn *et al.*, 1998).

In the past, parameterizations of atmospheric moist processes have been developed by dividing cumulus clouds into two groups, non-precipitating and precipitating (Frank, 1983). The former are shallow clouds that have a vertical depth of about 3 km, while precipitating clouds extend vertically into the middle- and upper-troposphere, and often form in very unstable atmospheres (Zawadzki *et al.*, 1981; Frank, 1983). Parameterizations of shallow clouds usually assume that these clouds are triggered by Rayleigh-Bénard convective instability (*i.e.*, turbulent-scale processes (Wetzel and Boone, 1995)). Parameterizations of deep clouds, for the most part, relate the triggering of these clouds to large scale forcings, *e.g.*, the magnitude of the grid-scale moisture convergence (Kain and Fritsch, 1992).

Rogers and Fritsch (1996) discuss a relatively new type of triggering function that includes the impact of landscape generated mesoscale circulations on the triggering variables. They estimate the magnitude of the largest subgrid-scale vertical velocity perturbation originating in each layer, and then calculate whether this perturbation is strong enough to overcome the total grid- resolvable negative inhibition between the source layer and the level of free convection. The work of Rogers and Fritsch (1996) is an important step in the process of developing a cumulus parameterization that is sensitive to the scale of the surface heterogeneity. However, they ignore subgrid-scale temperature and moisture perturbations forced by the landscape heterogeneity.

Here, we use a high resolution cloud resolving model to simulate the atmospheric response to heating of landscape patches (described in Section 2). The purpose is multifold: i) To suggest a new approach to the triggering of landscape generated moist convection, and ii) to identify an appropriate set of triggering variables. (iii) Analyze the impact of landscape and atmospheric forcings on the triggering variables, and iv) show that the triggering variables relate well to the distribution of rainfall. v) Obtain mesoscale and turbulent components from the high resolution simulated data, and vi) calculate various flux terms in budget equations for the parcel's temperature and moisture. Then, to address the closure problem, an analysis of terms in budget equations shows which of the terms in these equations need to be parameterized. Finally, vii) Develop a parameterization for these terms, as well as the mesoscale contribution to the parcel's vertical velocity. These subjects are discussion in Section 3. A summary and conclusion is present in Section 4.

2 Method

2.1 Numerical Model

A data set derived from observations that could be used for a study of the type presented here does not exist. Such a study requires very high resolution data over a relatively large area (1000 km^2). Fortunately, recent improvements in computer power have made possible a large number of high resolution model simulations. Some of these simulations have been applied to the study of convective processes over heterogeneous land surfaces (Nichols *et al.*, 1991; Chen and Avissar, 1994; Doran and Zhong, 1995; Fankauser *et al.*, 1995; Avissar and Liu, 1996; Lynn *et al.*, 1998). Still, we note that observations like those with aircraft (*e.g.*, Young, 1987, 1988; Finkele *et al.*, 1995; Mahrt *et al.*, 1994; Sellers *et al.*, 1995) and Doppler radar (Houze, 1989) can provide the data required to verify model derived results and parameterizations.

The model used in this study is the Goddard Cumulus Ensemble Model (GCE; Tao and Simpson, 1993). Briefly, the Rutledge and Hobbs (1984) scheme was used here to parameterize cloud microprocesses; the model uses a prognostic equation for the turbulent kinetic energy based on work by Deardorff (1975), Klemp and Wilhelmson (1978), and

Soong and Ogura (1980); and the model includes PLACE (Parameterization for Land-Atmosphere Convective Exchange), described by Wetzel and Boone (1995).

2.2 Experimental Domain

The experimental domain had a 250×250 m^2 horizontal grid resolution with periodic lateral boundary conditions, and a stretched vertical coordinate (see Table 1 for more details). Each simulation was run for 12 hours with a time step of 5 seconds. The total domain size was 512 grid-elements in the west-to-east direction (or 128 km) and 32 grid-elements in the north-to-south direction (8 km).

Two soundings on July 27^{th}, 1991, one located on the east coast and one located on the west coast of Florida, were taken from CaPE (the Convection and Electrification Experiment). They were averaged to obtain a mean sounding for an east-west cross section over the peninsula at 6 LST (Fig. 1). The sounding had a small initial convective available potential energy (CAPE)[2] of 740 kJ kg^{-1}, but a relatively low lifting condensation level pressure (an LCL of 1010 mb with a surface pressure of 1018 mb), low level of free convection (LFC: 839 mb), and high equilibrium level (EL: 190 mb). The vertical profile of the u-component of the wind is shown in Fig. 1b (the v-component was set equal to zero simply because we would expect it to have no important effect on the developing mesoscale circulations in the "truncated" north-to-south domain used here). The speed of the u wind in the lower troposphere is small enough to allow for the development of landscape generated mesoscale circulations, but large enough to affect this development (see below). Upon moistening of the planetary boundary layer (PBL), the initial sounding was conducive to the development of deep moist convection.

We initialized the numerical model with a uniformly distributed homogeneous vegetation consisting of a broad-leaf and coniferous forest. The stomatal resistance of the vegetation is a strong function of soil moisture in the root zone. For this reason, the soil moisture of sandy-clay-loam was chosen to "control" the surface distribution of land surface fluxes, leading to the generation of mesoscale circulations in our simulated domains. The process by which landscape circulations are generated by contrasting patches of wet and dry ground has been described in detail by Pielke *et al.* (1991), Avissar and

[2]The CAPE was calculated using a mixed layer depth from the land surface to 500 m.

Chen (1993), and Lynn *et al.* (1995a). We will not discuss this further and the reader is referred to these papers for further details.

Seven land surface domains were used here to provide the surface boundary conditions. In each, there were (different) alternating distributions of patches of dry and wet ground. In the dry ground, the volumetric soil moisture was chosen to be 10% of the fraction of the difference between field capacity and wilting point[3]. Here, this corresponds to a soil moisture, $\theta_{sl} = 0.153$. In the wet ground, this fraction was set at 90% of field capacity ($\theta_{sl} = 0.282$). Superimposed on each grid element was a random value of volumetric soil wetness, r, which was $-0.02 \leq r \leq 0.02$. Land surface patches with $\theta_{sl} = 0.153$ are referred to as "dry patches," while land surface patches with $\theta_{sl} = 0.282$ are referred to as "wet patches."

Four of the seven domains are shown in Fig. 2, and are labeled Domain 1 – Domain 4. In the main body of the text, we discuss in detail only results from Domain 1 and Domain 3, while in the Appendix we also refer to Domains 2 and 4. In Domain 1, there is a 64 km dry patch surrounded by two 32 km wet patches. Because the domain is periodic, there is actually a 64 km dry patch and 64 km wet patch in this domain. Note, the patches within the domains vary only in the west-to-east direction. In comparison, there were a number of differently sized dry patches in Domain 3. They are (left to right) 7.5 km, 4 km, 16 km, 4 km, 8 km, 20 km, and 4 km in length. Domain 2 contains patches of intermediate size, while Domain 4 contains very small patches. A summary of all domains used in this study is in Table 3. All domains are idealized representations of those that occur *in situ*. Still, the range of idealized domains chosen provides useful simulation results from which to draw conclusions about the potential impact of *in situ* landscape discontinuities on moist convection. In fact, the simulated impact of the landscape on the organized mesoscale flow was similar to that of Wang *et al.* (1998), who used a statistical parameterization of the land surface heterogeneity.

[3]Wilting point is the moisture content corresponding to matric potential of -15 bar, it is close to the volumetric water content at which plants can no-longer extract water from the soil. The field capacity is the volumetric water content corresponding to a balance that occurs in wet soil between diffusion (up) and gravitational drainage (down).

2.3 Numerical Experiments

There were a number of experiments produced for this work. Seven simulations were produced using domains of various sizes with moist processes "turned on" (Exp. 1w - Exp. 7w). These simulations were produced with the observed temperature and moisture sounding, and a background, westerly wind (constant with height) of 0.5 m s^{-1}. Four more simulations were produced with the observed sounding, including the observed wind profile shown in Fig. 1b (Exp. 8w - Exp. 11w). Two simulations were produced using Domains 1 and 3, but with moist processes "turned off" and the constant background wind (Exp. 1, and Exp. 2). We produced two additional simulations with moist processes turned off and the observed wind sounding shown in Fig. 1b (Exp. 3 and Exp. 4). By the phrase turned-on, we mean that clouds were allowed to form when model-grid elements reached supersaturation. By turned-off, we mean that no clouds were allowed to form in the simulated domain, and the atmosphere was allowed to super-saturate. Six additional simulations were produced with various initial boundary conditions. The reader can refer to Table 3 for more details.

2.4 Budget Equations

Any model variable ϕ can be separated into a resolved and sub-resolvable component:

$$\phi = \tilde{\phi} + \phi_s \tag{1}$$

where the $\tilde{\phi}$ represents the grid-scale, horizontal average at the large scale (*i.e.*, regional- or global-scale), and ϕ_s is the perturbation superimposed on it. We seek to develop a parameterization that can be used in regional- and global-scale atmospheric models. Thus, we assume that the flow component, ϕ_s, includes all motions on scales smaller than the synoptic flow.

We find it useful to decompose ϕ_s into mesoscale, ϕ', turbulent large eddy, ϕ'', and turbulent small eddy, ϕ''', components. Thus,

$$\phi_s = \phi' + \phi'' + \phi''' \tag{2}$$

Observations suggest that small, turbulent eddies have horizontal length scales of about 50 m, while turbulent large eddies have horizontal length sale of about 1 - 1.5 times the boundary layer height (H: Hardy and Ottersten. 1969: Konrad. 1970: Kaimal *et al.*. 1976: Caughey and Palmer. 1979: Taconet and Weill. 1983). The time-scale of these turbulent circulations is less than an hour. In comparison. mesoscale circulations have spatial scale of about 10 km – 200 km. and time-scale 50 min – 1 day (*e.g.*. Stull. 1988: Vidale *et al.*. 1997). Note. the decomposition of phi_s is independent of the grid-scale of the cloud resolving model.

We also assume that

$$\phi = \tilde{\phi} + \phi' + \phi'' + \phi''' \tag{3}$$

and

$$\langle \phi \rangle = \left\langle \tilde{\phi} + \phi' + \phi'' + \phi''' \right\rangle = \tilde{\phi} \tag{4}$$

where the angle brackets $\langle\rangle$ indicate an average of the variable ϕ (and its components) at the grid-scale of a regional- or global-scale atmospheric model.

If the flow is one-dimensional. the variables. $\tilde{\phi}$. ϕ'. ϕ''. and ϕ''' can be formally defined from a discrete fourier transform (*e.g.*. Walker. 1988) as:

$$\phi_j = \frac{1}{N} \sum_{j=0}^{N-1} \Phi_k e^{\frac{i2\pi jk}{N}} \tag{5}$$

such that:

$$\tilde{\phi} = \frac{1}{N}\Phi_o \tag{6}$$

$$\phi' = \frac{1}{N} \sum_{j=1}^{N_{\phi'}-1} \Phi_k e^{\frac{i2\pi jk}{N}} \tag{7}$$

$$\phi'' = \frac{1}{N} \sum_{j=N_{\phi'}}^{N_{\phi''}-1} \Phi_k e^{\frac{i2\pi jk}{N}} \tag{8}$$

$$\phi''' = \frac{1}{N} \sum_{j=N_{\phi''}}^{N-1} \Phi_k e^{\frac{i2\pi jk}{N}} \tag{9}$$

Here. $N_{\phi'-1}$ has a value that results in a filtering of both the large and small turbulent eddies from the data (*i.e.*. . the wavenumber $H/\Delta x$ - $1.5H/\Delta X$ (where Δx is the grid-spacing in the numerical model)). The field remaining after filtering is $\tilde{\phi} + \phi'$. from which ϕ' can be simply calculated. Likewise. the large eddies are found through the specification of an appropriate value for $N_{\phi''-1}$ (*i.e.*. $50\ \mathrm{m}/\Delta x$). In this case. the fields remaining would be $\tilde{\phi} + \phi' + \phi''$. Given both $\tilde{\phi}$ and ϕ'. ϕ'' can also be calculated.

To produce budget equations for θ_s and q_s, we write a simplified equation for the perturbation ϕ_s, ignoring molecular diffusion (Stull (1989)).

$$\frac{\partial \phi_s}{\partial t} + \bar{U}_j \frac{\partial \phi_s}{\partial x_j} + u_{j,s} \frac{\partial \tilde{\phi}}{\partial x_j} + u_{j,s} \frac{\partial \phi_s}{\partial x_j} = \left\langle \frac{\partial u_{j,s} \phi_s}{\partial x_j} \right\rangle + S_\phi \tag{10}$$

We then rewrite in flux form (we ignore horizontal advection of subgrid-scale quantities because we assume that circulations generated by patches are contained within each grid-element of the hosting model: *i.e.*, the regional- or global-scale model):

$$\frac{\partial \phi_s}{\partial t} + \frac{\partial \tilde{w} \phi_s}{\partial z} + \frac{\partial w_s \tilde{\phi}}{\partial z} + \frac{\partial w_s \phi_s}{\partial z} = \left\langle \frac{\partial w_s \phi_s}{\partial z} \right\rangle + S_\phi \tag{11}$$

We then expand each term (but the first and last) by substituting for ϕ_s. We have:

$$\frac{\partial \overline{\tilde{w} \phi_s}}{\partial z} = \frac{\partial \overline{\tilde{w} \phi'}}{\partial z} + \frac{\partial \tilde{w} \phi''}{\partial z} + \frac{\partial \tilde{w} \phi'''}{\partial z} \tag{12}$$

$$\frac{\partial w_s \tilde{\phi}}{\partial z} = \frac{\partial w' \tilde{\phi}}{\partial z} + \frac{\partial w'' \tilde{\phi}}{\partial z} + \frac{\partial w''' \tilde{\phi}}{\partial z} \tag{13}$$

$$\begin{aligned} \frac{\partial w_s \phi_s}{\partial z} = & \frac{\partial w' \phi'}{\partial z} + \frac{\partial w' \phi''}{\partial z} + \frac{\partial w' \phi'''}{\partial z} + \frac{\partial w'' \phi'}{\partial z} + \frac{\partial w'' \phi''}{\partial z} \\ & + \frac{\partial w'' \phi'''}{\partial z} + \frac{\partial w''' \phi'}{\partial z} + \frac{\partial w''' \phi''}{\partial z} + \frac{\partial w''' \phi'''}{\partial z} \end{aligned} \tag{14}$$

$$\begin{aligned} \left\langle \frac{\partial w_s \phi_s}{\partial z} \right\rangle = & \left\langle \frac{\partial w' \phi'}{\partial z} \right\rangle + \left\langle \frac{\partial w' \phi''}{\partial z} \right\rangle + \left\langle \frac{\partial w' \phi'''}{\partial z} \right\rangle + \left\langle \frac{\partial w'' \phi'}{\partial z} \right\rangle \\ & + \left\langle \frac{\partial w'' \phi''}{\partial z} \right\rangle + \left\langle \frac{\partial w'' \phi'''}{\partial z} \right\rangle + \left\langle \frac{\partial w''' \phi'}{\partial z} \right\rangle + \left\langle \frac{\partial w''' \phi''}{\partial z} \right\rangle + \left\langle \frac{\partial w''' \phi'''}{\partial z} \right\rangle \end{aligned} \tag{15}$$

Finally, we can use the above equations to obtain θ_o and q_o, that is, a triggering parcels potential temperature and specific humidity. This is done by substituting θ (and then q) for ϕ, and then averaging the equation for θ_o (and then q_o) over the area of a parcel. Note,

$$\phi_o = \overline{\phi'}^p + \overline{\phi''}^p + \overline{\phi'''}^p \tag{16}$$

where the superscript^p indicates an average over the area of the parcel.

3 Results

3.1 A New Approach To the Triggering Problem

In our opinion, two approaches have been suggested for triggering moist convection over heterogeneous land surface patches. The first approach assumes that the largest patch within a grid-scale domain produces the biggest sub-grid scale perturbations originating within each source layer (Rogers and Fritsch, 1996). The second approach, as suggested by Lynn *et al.* (1998), assumes that the size of the subgrid-scale perturbations should vary proportionally with the average size of the patches. In both, bigger patches should produce more rainfall than smaller patches because the perturbations over the former are larger than over the latter.

Landscape dry patches heat the overlying atmosphere more than wet patches heat the overlying atmosphere. As a result, the atmospheric pressure drops over the dry patch and mesoscale circulations can form on either side of the dry patch. These circulations moved inward over the dry patch. In our simulations, mesoscale circulations occuring over individual dry patches produced rainfall over these patches. This rainfall occurred usually between 10 and 14 LST.

We calculated the total accumulated rainfall from the simulations described in Table 3. We did so by integrating over the whole domain in time and space. A linear interpolation was then performed and the slope, y-intercept, and regression coefficient were obtained. The relationship between the domain averaged (accumulated) rainfall and average patch size was not monotonic (Table 4). We obtained similar results even when we used the largest patch size within each domain, instead of the average patch size. Thus, neither the first or second approach would appear to well represent the rainfall that can be triggered by landscape patches.

The reason that rainfall is not monotonic with average patch size is simple, and can be explained by two examples, shown in Fig. 3a (Exp. 1w) and Fig. 3c (Exp. 4w). After examining such figures, we can conclude that rainfall and its duration increase with increasing patch size[2]. However, isolated rain clusters can occur even over small patches.

[2]The forcing by the land surface depends upon the difference in heat flux between the wet and dry patches. Here, this difference at the time of rainfall formation was about 100 W m^{-2}, which can typically occur between different vegetation surfaces or in response to soil moisture differences (*e.g.*, Sun and Mahrt, 1994)

and domains (such as Domain 2) with small patches can have more patches (and hence more rainfall "clusters") than domains with large patches (such as Domain 1). Thus, the domain accumulated rainfall is a function of both patch size and patch number.

It may be obvious to the reader that accumulated rainfall depends upon both patch size and patch number: but it might not be obvious how to proceed in the development of a triggering function. However, the results show a simple, linear relationship between patch size and accumulated rainfall over *individual* patches (Fig. 4). In fact, the correlation coefficient was 0.99.

The modeled relationship between rainfall and individual patch size can be explained by reference to linear theory. In the absence of a background wind, linear theory has been used to simulate the coarse features of mesoscale circulations. Dalu *et al.* (1991) have shown that the intensity of the flow increases proportionally with increasing patch size, for patches of size less than the local Rossby radius of deformation.

Figures 3b and 3d show that the background wind profile can affect the development of rainfall over patches. A background wind increases turbulent dissipation, reducing, quite substantially, the generation of landscape generated rainfall over small patches. At the same time, a synoptic wind from a warmer to a colder surface can strengthen the horizontal temperature gradient - provided, however, that the patch size is large enough and the synoptic wind is less than a critical value - *e.g.*, 5 m s^{-1} (Pielke, 1984). Thus, rainfall over one side of the patch can increase in the presence of a background wind, as shown in Fig. 3b. Thus, the distribution over individual patches, such as in Exp. 8w (Domain 1), can be quite asymmetric, suggesting the need to represent a multiple of cloud populations over such patches. Still, the correlation coefficient for the set of experiments (Exp. 8w – Exp. 11w) was 0.95.

Note, the model had cyclic boundary conditions. It seems clear that some of the rain occurred over the small dry patches relatively late in the simulation because of the boundary conditions. This was because some of the convective cells crossed the right boundary and reentered the domain on the left side. Had we used open boundary conditions, the regression coefficient would likley have been even higher than obtained here.

The high correlation coefficient in both cases suggests the validity of a third approach. A more realistic approach to the problem would be to develop a trigger function to be applied to multiple, individual patches, whose associated variables would depend upon patch size (and atmospheric background conditions). The domain averaged quantities could then be obtained from a cloud model as the integral over the domain of the regional- or global-scale atmospheric model of cloud related variables occurring over individual patches.

3.2 Definition of Triggering Variables

As noted above, Rogers and Fritsch (1996) recognized that sea-breeze-like fronts associated with landscape generated mesoscale circulations can have parcels with strong (upward) vertical velocity. They empirically relate the size of the patches to the vertical velocity of the parcel, and use this velocity in their triggering function.

To identify an appropriate set of triggering variables that could be used in a new triggering function, we examined modeled atmospheric fields at various times during the model simulations. These atmospheric fields were the modeled perturbation fields of horizontal wind (u_s), vertical velocity (w_s), potential temperature (θ_s), and specific humidity (q_s). Our analysis indicated, like that of Rogers and Fritsch (1996), that the most robust parcels occur in parcels along sea-breeze like fronts. However, it also showed that the temperature and moisture of these parcels can be different than the grid-scale. Thus, vertical velocity, temperature, and moisture affected the triggering of moist convection.

For this reason, we propose a trigger function that includes the vertical profiles of velocity (w_o), as well as potential temperature (θ_o) and specific humidity (q_o). Here, the subscript zero means that the triggering variables refer to parcels moving along sea-breeze like fronts (note, the parcel is an area average of the subgrid-scale perturbations). It seems evident that a trigger function that uses each of these variables has the advantage that it provides the information required to determine if triggering of moist convection should occur, without refering to an inhibition energy (Rogers and Fritsch, 1996) or empirical relationships between the grid-scale and subgrid-scale (Fritsch and Chappell, 1980) Still, out approach is similar to Fritsch and Chappell (1980) and Rogers and Fritsch (1996), in that we seek to relate subgrid-scale properties to the triggering of moist convection.

This trigger function would be used as follows: i) The parcel's temperature and moisture would be used to calculate if saturation occurs on the subgrid-scale. In addition, the initial vertical velocity of this parcel at the level of saturation would be used to more realistically initialize a parcel's ascent. ii) Like Fritsch and Chappell (1980). The parcel would ascend upward because it is buoyant: if it reaches its level of free convection. then convection would occur. Note. the triggering variables have a vertical profile that extends from the surface to the top of the PBL. Thus the parcel would grow into an "environment" that could be quite different (more moist and cool) than the grid-scale. The other schemes do not include a vertical dependence in the subgrid-scale variables.

To obtain. $w_o(z)$. $\theta_o(z)$. and $q_o(z)$ for each dry patch. we first identified the location of the largest moisture perturbation along each front over each side of the patch. This became the center of our parcel for each frontal boundary. We then averaged w_s. θ_s. and q_s over surrounding grid-elements. to obtain parcels of square area (square areas were chosen here. rather than circular areas. out of convenience).

We examined the relationship between parcel size and the magnitude of the triggering variables. Figure 5 shows that there exists a strong sensitivity to the size of the parcel. but when the parcel size is either 10.6 or 18.1 km^2. its vertical profiles resemble those of the surrounding PBL (not shown). For our purposes. we chose the averaging size to be four grid elements. or a parcel of size 5.1 km ^{2} (9×9 grid-elements). This size is consistent with the area of observed cloud bases. and those utilized in cumulus convection schemes.

3.3 Impact of Initial Conditions on Triggering Variables

We utilized a number of simulations with moist processes turned off. to study the dependence of the vertical profiles of the triggering variables on initial conditions.

3.3.1 Sensitivity To Patch Size and Background Wind

In Exps. 1w and 4w. the rainfall occurred most intensely over bigger patches than small patches. To see why. we examined the triggering variables obtained with the same patch sizes. but with moist processes turned off (Exp. 1 and Exp. 2). When we averaged the triggering variables in Exp. 1 and Exp. 2 over this time period. we noted that. for the most part. the triggering variables over patches of different sizes had similar magnitude (Fig. 6). Yet. differences were obtained in rainfall over the different patches. Clearly. the vertical depth of the triggering variables had an impact on rainfall. This vertical depth reflects the relative robustness of the mesoscale circulations over each patch.

In Exp. 8w and 11 w. the background wind (*i.e.*. the observed sounding) had strong effect on rainfall. To see why. we examined results from Exp. 3 and 4. which have the same patch sizes as Exp. 8w and 11w. but moist processes were turned off. Figure 7 shows the vertical profiles of the triggering variables along the downwind side of each dry patch (also between 10 - 14 LST). We show these profiles. rather than the profiles on the upwind side of the patches because rainfall was most intense along this side of the various patches. In this case. both the magnitude and vertical depth of the triggering variables depended upon patch size.

A background wind increases the turbulent dissipation of the atmospheric gradient in temperature between the dry and wet patches. Over small patches. this dissipation was sufficient to reduce the magnitude of the triggering variables. even over the downwind side of each patch. Thus. in Exp. 11w. the peak values of rainfall over the smaller patches were much less than in Fig. 4w.

However. as noted above. a synoptic wind from a warmer to a colder surface can. if the dry patch is large enough. strengthen the horizontal temperature gradient. This can enhance the frontal forcing at the downwind patch boundaries. This affect is present in Exp.3. and was reflected in the rainfall distribution of Exp. 8w.

To emphasize this point. Figure 8 provides a comparison of triggering variable results obtained on the upwind and downwind side of the dry patch in Exp. 3. It shows that the background had a detrimental effect on the triggering variables on the upwind side of the patch (the westward (left) side). This is because a synoptic wind direction from a colder to a warmer surface weakens the horizontal temperature gradient. Thus. the set of triggering variables obtained over a individual patch can depend upon the direction and magnitude of the background wind. We will show that it is useful to include such information in a parameterization of moist convection.

3.3.2 Impact of Surface Forcing, Atmospheric Stability, Specific Humidity, and Latitude

In Exp. 5. we examined the impact of the soil moisture gradients upon the triggering variables (Fig. 9). The changes in soil moisture of the dry and wet patches affected the horizontal contrast in surface sensible heat fluxes. and subsequent vertical. turbulent transfer of heat and moisture (not shown). This led to relatively less robust mesoscale circulations than in Exp. 1 (the control experiment), and a decrease in the magnitude of the triggering variables. These variables decreased roughly proportionally with a decrease in the standard deviation of the surface sensible heat fluxes (not shown). Lynn *et al.* (1995b) also found a similar relationship between the mesoscale heat fluxes and the standard deviation of the surface sensible heat flux.

In Exp. 6, we increased the atmospheric stability of the sounding. The new sounding was typical of a summertime day with strong subsidence occurring within a strong high pressure system. This impacted both the surface fluxes and atmospheric turbulent fluxes, reducing the depth of the vertical mixing when compared to Exp. 1. The change in stability strongly effected the vertical depth of the triggering variables.

Moreover, the magnitude of w_o obtained in Exp. 6 was much less than obtained in Exp. 1. The variable w_o is highly sensitive to the turbulent convection, which depends strongly on the stability. However, the vertical convergence of the heat fluxes determines the vertical structure of θ_o and q_o. Here, these fluxes converged over a more shallow layer than in Exp. 1. Thus, θ_o and q_o were affected less by the change in stability than w_o.

The percentage change in the initial profile of the domain average specific humidity, $\bar{q}$, was simply proportional to the change in q_o (Exp. 7). Moreover, the change in $\bar{q}$ led to a decrease in the sensible heat fluxes from both dry and wet patches, which had a negative impact on the development of mesoscale circulations. Thus, the change in $\bar{q}$ also affected the magnitude of the vertical profiles of w_o and θ_o: each was smaller than in Exp. 1.

The change in latitude had relatively little effect on the triggering variables (Exps. 8 and 9). The patches were too small to allow for a significant impact of the Coriolis force on the triggering variables.

3.4 Relationship between Triggering Variables and Moist Processes

Above, we showed that the vertical depth and magnitude of the triggering variables corresponded to the intensity of rainfall over patches of different sizes. We did so by comparing profiles of the triggering variables from simulations without moist processes, and surmised that the results obtained in those simulations would apply to simulations with moist processes. Yet, it is useful to look in more detail at the relationship between rainfall and the triggering variables, using results from simulations with moist processes. We can provide further support for the previous conclusions, as well as emphasize additional particulars of this relationship. To limit the length of the discussion, we show only vertical profiles of q_o.

The growth and decay in the vertical profiles of q_o corresponded quite well with the growth and dissipation of rainfall in each experiment (Fig. 10). Similar results were obtained for w_o and θ_o (not shown). In addition, the time-scale of the triggering variables obtained over Patch #2 and #5 in Exp. 4w were much less than Exp. 2. Similarly, rainfall grew and decayed more quickly over these patches than over larger patches.

In addition, the time scales over Patch #2 and #5 were short enough to lead to a growth of q_o, its dissipation, and then regrowth of q_o (Fig. 10c, d) over these patches. In contrast, the growth and dissipation of the triggering variables over the larger patches took longer than over the smaller patches. Similarly, the rainfall occurred over these patches for a longer time period than over the smaller patches.

Figure 11 shows that the triggering variable q_o grew in size more quickly than its counterpart on the upwind side of the dry patch (Exp. 8w). The differences in q_o obtained on the upwind and dowin wind side of the dry patch corresponded with differences in rainfall shown in Fig. 3b on each side of this patch.

Prior to the formation of moist convection, the trigger function variables are associated with mesoscale circulations that are forced solely by the land surface patches. After the formation of moist convection, however, these circulations can be extensively modified by moist convection, *e.g.*, by cloud shading of the surface, and evaporative cooling along the sea-breeze-fronts (Lynn *et al.*, 1998). A comparison of Figures 10 and 11 with Figs 6 and 7 show the impact of these processes on the triggering variables. Moreover, turbulent processes occurring within clouds can transfer heat and moisture upwards into middle troposphere. These proceses also affect the vertical profiles of the triggering variables.

Cloud shading also weakens the forcing on the developing mesoscale circulations. However, evaporative cooling counteracts, in part, the impact of cloud shading on the developing circulations (Lynn *et al.*, 1998). It also accelerates the movement of the fronts inward towards the center of the dry patch. Thus, mesoscale circulations affected by moist processes have a shorter time-scale than those unaffected by moist processes. A more thorough discussion of this issues is beyond the scope of this paper.

3.5 Budget Equations

We analyzed the budget equations using the data set described in the Appendix. The Appendix describes how the modeled data were separated into mesoscale (ϕ') and large-eddy (ϕ'') perturbations. We did not obtain ϕ''' from that modeled data because the resolution of this data was much bigger than the horizontal length scale of these eddies. Note, the model's parameterization for turbulence represents small eddy processes, and, of course, a proportion of the unresolved exchange due to large eddies. Conversely, large eddy fluxes calculated with the filtered fields might include contributions from small eddies.

Because we are unable to obtain the small eddy perturbations, we have a simplified budget equation for ϕ_s.

$$\frac{\partial \overline{\tilde{w}\phi_s}}{\partial z} = \frac{\partial \overline{\tilde{w}\phi'}}{\partial z} + \frac{\partial \overline{\tilde{w}\phi''}}{\partial z} \tag{17}$$

$$\frac{\partial \overline{w_s\tilde{\phi}}}{\partial z} = \frac{\partial \overline{w'\tilde{\phi}}}{\partial z} + \frac{\partial \overline{w''\tilde{\phi}}}{\partial z} \tag{18}$$

$$\frac{\partial \overline{w_s\phi_s}}{\partial z} = \frac{\partial \overline{w'\phi'}}{\partial z} + \frac{\partial \overline{w'\phi''}}{\partial z} + \frac{\partial \overline{w''\phi'}}{\partial z} + \frac{\partial \overline{w''\phi''}}{\partial z} + \frac{\partial \overline{w'''\phi'''}}{\partial z} \tag{19}$$

$$\left\langle \frac{\partial w_s\phi_s}{\partial z} \right\rangle = \left\langle \frac{\partial w'\phi'}{\partial z} \right\rangle + \left\langle \frac{\partial w'\phi''}{\partial z} \right\rangle + \left\langle \frac{\partial w''\phi'}{\partial z} \right\rangle + \left\langle \frac{\partial w''\phi''}{\partial z} \right\rangle + \left\langle \frac{\partial w'''\phi'''}{\partial z} \right\rangle \tag{20}$$

where the overline indicates a Reynold's average over the time- and -spatial scale of the small eddies. Note, the Reynolds assumption implies that the fluxes $\overline{\tilde{w}\phi'''}$, $\overline{w'''\tilde{\phi}}$, $\overline{w'\phi'''}$, $\overline{w'''\phi'}$, and $\overline{w''\phi'''} = 0$. A test of these equalities is not formally presented here, and is left for interested parties. However, we note that the parameterized turbulent fluxes were large only in the lowest part of the PBL. This suggests that the cross terms described above are indeed small above the lower PBL, and that the calculated large-eddy perturbations do indeed represent the large-eddy variables that might occur *in situ*.

Fig. 12 shows the vertical profiles of various terms in the budget equation, obtained in Exp. 3. We chose Exp. 3 because it used the observed sounding (with the u wind), which is, perhaps, more typical than a light-wind case. In the budget equations, there are a number of fluxes for which parameterizations do not yet exist. Yet, there is a need to develop a parameterization for only $\overline{w''\theta'^{p}}$ and $\overline{w''q'^{p}}$. These terms are the vertical transport of the mesoscale temperature and moisture by the turbulent wind. New parameterizations for other terms not previously described in the literature were found not to be required. *e.g.*, $\overline{w'\theta'}^p$, because these terms were relatively small.

These results can be explained through an analysis of Figure 13, which shows the vertical profiles of the mesoscale and large-eddy perturbations obtained in Exp. 3. It is for a "triggering" parcel moving upwind (east-to-west), with an upwind moving sea-breeze-like front. The data were averaged over the time period 10 - 14 LST. Quite simply, $w'' >> w'$, while $\theta'' << \theta'$, and $q'' << q'$.

Figure. 14 shows the vertical profiles of the fluxes in the budget equations, but for those obtained in Exp. 8w. A careful examination of this figure suggests the following: i) Both $\overline{w''\theta'}^p$ and $\overline{w''q'}^p$ again contribute most significantly to the triggering of moist convection. ii) The vertical structure of these curves remained relatively unchanged, thus, we can develop a single parameterization for both $\overline{w''\theta'}^p$ and $\overline{w''q'}^p$ that should work prior to and during the formation of clouds. iii) Both $\overline{w''\theta''}^p$ and $\overline{w''q''}^p$ force the vertical transport of heat and moisture within the cloud. iv) These terms, which represent the vertical transport of the turbulent potential temperature and moisture, can be parameterized using conventional cumulus cloud parameterizations. Table 5 shows a listing of terms that occur in the budget equations. It also shows which of these terms are required to obtain the vertical profiles of θ_o and q_o.

The results obtained above were found to apply to other experiments produced as part of this work. Therefore, we believe the conclusions reached to be valid for initial conditions other than those examined here. Note, we do not show in any of our figures the fluxes $\langle w'''\theta'''\rangle$, $\langle w'''q'''\rangle$, or $\overline{w'''\theta'''}^p$, $\overline{w'''q'''}^p$ but these contributed significantly to the vertical profiles of θ_o and q_o within the surface layer and lowest 100 or so meters of the PBL. Nor, do we show the vertical profiles of S_θ or S_q. Each should be obtained as a residual of the cloud parameterization.

3.6 Parameterization

We made a thorough examination of model results obtained in the previous experiments. We concluded that the method suggested by Lynn *et al.* (1995b) should be used to obtain parameterizations for the needed terms. The reason being that the parameterized fluxes (and $\overline{w'^2}^p$) have a time-scale different than the turbulent fluxes. Thus, to realistically describe the evolution of the fluxes requires a prognostic equation for them, rather than a diagnostic relationship between them and the surface (and atmospheric) forcing. We applied Buckingham Pi theory to obtain the dimensionless numbers for the parameterization (Stull. 1988).

A Chebyshev polynomial has been used to describe the vertical structure of the following dimensionless numbers:

$$D_{\overline{u''\theta''^p}} = \frac{\overline{u''\theta'^p}}{f(U, U_o)\Theta} \tag{21}$$

$$D_{\overline{u''q'^p}} = \frac{\overline{u''q'^p}}{f(U, U_o)Q} \tag{22}$$

$$D_{\overline{u'^p}} = \frac{\overline{u^p}}{f(U, U_o)} \tag{23}$$

We then obtain the coefficients of the polynomials for each from a prognostic equation:

$$\frac{dc_k}{d\tau} = -\alpha_k D_1 D_2 - c_k \beta_k \tag{24}$$

where α_k. and β_k are empirical parameters deduced from the experimental (numerical) data set. and τ is linearly related to the time of day t.

The coefficients are determined by solving numerically Eq. 24 in two steps. using a "time-splitting" technique (*e.g.*, Pielke. 1984). In the first step. intermediate coefficients c_k^* are calculated using an explicit scheme.

$$c_k^*(\tau + \Delta\tau) = c_k(\tau) + \Delta\tau\alpha_k D_1 D_2 \tag{25}$$

and in the second step. the c_k are calculated using an analytical solution:

$$c_k(\tau + \Delta\tau) = c_k^*(\tau + \Delta\tau)\epsilon^{(\Delta\tau\beta_k)} \tag{26}$$

To represent the residual impact of the heat fluxes on the PBL. D_1 as an e-folding time of three hours. Note. we have a set of three c_k. c_k^u. $c_k^{u''\theta'}$. and $c_k^{u''q'}$. as well as a set of three α_k. which are α_k^u. $\alpha_k^{u''\theta'}$. and $\alpha_k^{u''q'}$. We refer to only one β_k. where

$$\beta_k = \frac{1.}{10800.x^{0.25}} \tag{27}$$

Here. $x = R_i/\mathbf{L}$.

The dimensionless number D_1 consists of:

$$D_1 = \frac{\Delta u'''\theta'''}{f(U, U_o)\Theta} \tag{28}$$

while D_2 is:

$$D_2 = f(R_o, \mathbf{L}) \tag{29}$$

The Appendix describes the form of the parameterization in more detail. Table 6 has a listing and description of all variables used in the parameterization, and Table 7 has a listing of the empirical coefficients a_k.

We used model output to obtain the complete set of dimensionless numbers. The sensitivity of the dimensionless numbers, including the fluxes and mesoscale vertical velocity, to changes in surface and atmospheric variables was similar to that obtained for the mesoscale heat fluxes by Lynn *et al.*, 1995b. The reader is referred to their work for more details. Instead, we only present Fig. 17 and 18, which shows the vertical profiles of $D_{\overline{u''\theta'^p}}$, $D_{\overline{u''q'^p}}$, and $D_{\overline{u'^p}}$ from the model output and the parameterization for each.

These figures demonstrate the ability of the parameterization to represent the sensitivity of the model results. However, the magnitude of the fluxes obtained were less than simulated by the model. This is because of the non-linearity of the fluxes (w'' varies chaotically in time). Still, the parameterization captured the most important features of the observed data set: i) the dependence upon patch size, ii) background wind, iii) stability, and iv) specific humidity. Other cases from the experimental data are not shown, but were independently tested to insure that the parameterization for each variable is robust.

4 Summary and Conclusion

A set of relatively high resolution three-dimensional (3D) simulations were produced to investigate the triggering of moist convection over heterogeneous land surface domains. This moist convection was triggered by mesoscale circulations generated by the landscape heterogeneity. We found that a monotonic (linear) relationship exists between the *local* accumulated rainfall over *individual* patches and the size of these patches, but not the *domain* accumulated rainfall and domain averaged patch size. Thus, we suggest that cumulus parameterizations and their trigger functions for heterogeneous landscapes should be applied over multiple, individual patches within the domain, rather than to a single patch of average size.

An appropriate set of triggering variables for this triggering function consists of the vertical profiles of vertical velocity, temperature, and moisture, for parcels moving along sea-breeze like fronts associated with landscape generated mesoscale circulations. We suggest a simple trigger function using these variables, which uses the principles described by Fritsch and Chappell (1980) and Rogers and Fritsch (1996).

The triggering function variables were found to be sensitive to the surface contrasts in sensible heat flux, atmospheric stability, initial profile of atmospheric moisture, and moist (cloud) processes. They were relatively insensitive to latitude, but showed that background wind could impact the magnitude of the triggering variables, as well as create important differences between triggering variables over individual patches. We noted that the evolution of the triggering variables prior to and during the development of moist convection described quite well the local distribution of rainfall over patches.

We derived budget equations for θ and q_o. These equations contain contributions from mesoscale and turbulent fluxes, as well terms such as $\overline{w''\theta'^p}$ and $\overline{w''q'^p}$ (which represent the turbulent vertical flux of the mesoscale temperature and moisture perturbation, respectively). We used a Fourier transform to filter the data, and obtain a distribution of mesoscale and turbulent perturbations. Using this new data set, we then calculated the various terms in the budget equations, and determined that $\overline{w''\theta'^p}$ and $\overline{w''q'^p}$ need to be parameterized to close each respective equation. Quite interestingly, parameterizations developed for cases without clouds should also apply to cases with clouds, since the vertical structure of these terms remained relatively unchanged by moist processes.

It might be interesting to the reader to note that the grid-scale mesoscale fluxes are also insensitive to phase transitions. Therefore, the parameterizations developed by Lynn *et al.* (1995b) and Zeng and Pielke (1995) should also apply as given for both dry and moist regimes.

As noted, a linear relationship was obtained between rainfall and patch size. Perhaps, if moist convection had occurred later in the simulation, the relationship found would have a more exponential shape (increasing non- linearly upward with increasing patch size). This is because non-linear advective affects become more important relative to linear processes as mesoscale circulations develop and move inward over the domain. Moreover, we would expect that the maximum rainfall would occur for patch sizes equal to the local radius of deformation (*e.g.*, Lynn *et al.*, 1998). The sizes of patches simulated here were all less than the local radius.

We used similarity theory to parameterize $\overline{w''\theta''}$ and $\overline{w''q''}$ and w'. The important variables that were incorporated into a parameterization are the patch size (and local radius of deformation), gradient in the surface sensible heat fluxes, the background wind, planetary boundary layer height, and planetary boundary layer atmospheric potential temperature and specific humidity. These variables were used to develop empirical relationships between them, the fluxes, and the mesoscale vertical velocity.

Finally, the development and dispensation of data sets such as FIFE and LBA can provide additional evaluation and refinement of the parameterizations suggested in this work.

5 Appendix

5.1 Filtering the Modeled Data

To analyze the budget equations, we needed to obtain from the modeled data the mesoscale and turbulent fields. Observations suggest that turbulent eddies have horizontal length scales of about 1 - 1.5 times the boundary layer height (Hardy and Ottersten, 1969; Konrad, 1970; Kaimal *et al.*, 1976; Caughey and Palmer, 1979; Taconet and Weill, 1983). It is a simple task to calculate the boundary layer height, and then obtain the appropriate wavenumber for filtering the data. Note, Table 8 contains a summary of definitions used in this section and elsewhere in this paper.

We calculated the boundary layer height across the domain and used the maximum boundary layer height to obtain a filtering wavenumber for the mesoscale fields. We then examined the vertical profiles of the triggering variables obtained after assuming that turbulent eddies have wavelength from 1.5 to 3.5 (in increments of 0.5) times the boundary layer height (H). The distribution of the atmospheric fields were most sensitive to filtering in the range of values $1.5H$ - $2.5H$. However, the distribution of the filtered fields did not change very much when we used a wavelength of $3.0H$ or $3.5H$. This implies that when we used, for example, a wavelength of 3.0 times the boundary layer height, that this value enabled a filtering of the large-eddies from the modeled data, leaving the mesoscale fields.

To support this supposition, we did a spectral analysis (Fig. 15), using the domains shown in Fig. 2. This analysis revealed that the dominant spectral energy (in the u-wind field) corresponds to the wavenumber of the surface forcing. For example, peaks in the power spectrum occurred, for example, for wavenumber 4 (*e.g.*, Patch = 3: a 32 km dry-wet patch couplet) and wavenumber 7 (Patch #5: a 18 km couplet). Most importantly, a simulation of very small patches (≈ 0.25 m^2: Domain 4), produced an energy spectrum with wavelengths smaller than about 10 km. The energy associated with wavelengths greater than 10 km, was mesoscale-kinetic energy (Avissar and Chen, 1993). It corresponds to the set of mesoscale perturbations derived from the initial data set. In contrast, turbulent kinetic energy occurred in association with wavelengths less than 10 km. This energy corresponds with the large eddy perturbations. Note, the scale-separation between the two regimes depends upon patch size.

Based upon the prior analysis, we adopt a wavelength of $3.0H$ to filter the data. The value of $3.0H$ obtained from our simulations differs from the range $1H$ - $1.5H$ suggested by observations. This is because the model simulations used a relatively coarse resolution to resolve the turbulent fields. As noted, the smallest eddies that the model could resolve with a minimum of two grid-elements corresponded to a wavelength of 500 m. This is much larger than the typically observed wavelength for the small eddies.

Figure 16 shows an example of filtered atmospheric fields obtained in Exp. 3. The mesoscale horizontal wind (u'), potential temperature (θ'), and specific humidity fields q' corresponded very well with observations of sea-breezes and sea-breeze-like circulations produced with mesoscale models (*e.g.*, Finkele *et al.*, 1994; Lynn *et al.*, 1995a). However, the model simulated vertical wind field was "contaminated" by the buoyancy forcing associated with turbulent motions. After filtering in space (and time) the modeled vertical velocity field, we could not obtain a meaningful mesoscale vertical velocity field. For this reason, we do not show this field in Fig. 16.

Instead, we note that the hydrostatic assumption applies when the ratio of the vertical to the horizontal length scale of the circulation is equal to or less than one (Pielke, 1984). Thus, we believe it justified to assume that the derived mesoscale fields were hydrostatic. Moreover, the mesoscale vertical velocity field obtained from the mesoscale horizontal wind (using the continuity equation) corresponded well with results obtained from mesoscale models and obtained indirectly through the use of observations. We show this derived field in Fig. 16b, and obtain the vertical velocity in all experiments from the continuity equation.

As described previously, Fig. 13 shows vertical profiles of the mesoscale and turbulent perturbations obtained for the triggering parcels in Exp. 3. The relatively robust mesoscale perturbations occurred in this experiment because of the contrast in turbulent transport between the dry and wet patches, and horizontal and vertical advection associated with the mesoscale circulations. In contrast, turbulent, large eddies formed because of buoyancy forcing. Near the ground, the difference between these eddies and their surroundings was relatively small. Hence, the magnitude of their perturbations near the ground was relatively small compared to the mesoscale perturbations. In the upper PBL large eddy thermals are relatively cool and moist when compared to entraining air from the capping inversion from above the mixed layer. This entrainment generated more significant turbulent eddy perturbations in the upper PBL than occurred in the lower PBL.

For the purposes of the analysis, we also obtained the turbulent, large eddy fields. For brevity, these are not shown. However, $\phi'' = \phi_s - \phi'$.

5.2 Equations for Parameterization

The dimensionless number, D_1 is defined as follows:

$$D_1 = \frac{\Delta w'''\theta'''}{f(U, U_o)\Theta} \tag{30}$$

The dimensionless variable $\Delta w'''\theta'''$ is used to represent the relative forcing by the land surface. The bigger it is, the stronger this forcing. It increases with the growth in the difference in sensible heat flux between patches, but decreases when $U > U_o$.

The function $f(U, U_o)$ is defined for two types of parcels: those moving with the prevailing wind ($f(U, U_o^u)$) and those moving against the prevailing wind ($f(U, U_o^d)$). To obtain $f(U, U_o^u)$, we first define the ratio of U to U_o^u, where U is the background wind and U_o^u is a constant $= 1.0$ m s^{-1}.

$$x^u = \frac{U}{U_o^u} \tag{31}$$

Then, for parcels moving with the prevailing wind:

$$\begin{aligned} f(U, U_o) &= [1\text{m s}^{-1}] \qquad (U < U_o^u) \\ f(U, U_o^u) &= \frac{[1\text{m s}^{-1}]}{x^u 2.718^{(1-x^u)}} \quad (U \geq U_o^u) \end{aligned} \tag{32}$$

To obtain $f(U, U_o^d)$, we also define the ratio of U to U_o^d, where U_o^d varies as a function of patch length. To obtain this functional relationship, we made additional simulations with Domain 1 (Table 3). In one case, a sea-breeze-like front was nearly stationary over the downwind side of the dry patch. Here, the background wind (in the PBL) was about 4 m s^{-1}. Most interestingly, the vertical velocity of the vertical wind perturbation at this stationary front (prior to the convergence of the fronts) was most robust of any of the simulations. Bechtold *et al.* (1991) discuss the reasons why stationary sea breezes produce the most robust vertical velocities. To simplify the application of their results to the parameterization, we simply assume that U_o = 6.25E-5 s^{-1}**L** (= 4 m s $^{-1}$ for Domain 1). The dependence of U_o on patch size allows for the impact of turbulent mixing on the horizontal gradient in temperature. Thus, we have:

$$x^d = \frac{U}{U_o^d} \tag{33}$$

For parcels moving against the prevailing wind:

$$\begin{aligned} f(U, U_o^d) &= [1\mathrm{m\ s}^{-1}] & \mid U < U_o^d \\ f(U, U_o^d) &= \frac{[1\mathrm{m\ s}^{-1}]}{x^u 2.718^{(-0.25 x^{u4})}} & \mid U \geq U_o^d \end{aligned} \tag{34}$$

For D_2, we define the variable x as:

$$x = \frac{R_o}{\mathbf{L}} \tag{35}$$

and $0 \leq x_o \leq 1$ Note, the variable R_o is a local radius of deformation (see Lynn *et al.*, 1998). The frictional dissipation variable in the equation for R_o was determined to be three-hours from an examination of the mesoscale kinetic energy obtained with the cumulus ensemble model.

For all c_κ^u

$$D_2 = x_o \sin\left(1.57 x^{0.333}\right) \tag{36}$$

For $c_\kappa^{\overline{u''\theta'^p}}$

$$d_1 = x_o \sin\left(1.57 x^{0.60}\right)$$
$$d_2 = x_o \sin\left(1.57 x^{0.333}\right)$$
$$d_3 = x^{0.5}$$

$$d_4 = d_2$$
$$d_5 = d_2$$
$$(37)$$

For $c_k^{\overline{w''q'^p}}$.

$$d_1 = x_o \sin\left(1.57 x^{0.25}\right)$$
$$d_2 = x_o \cos\left(1.57\sqrt{x}\right)$$
$$d_3 = x_o \sin\left(1.57 * x^{0.333}\right)$$
$$d_4 = d_2$$
$$d_5 = d_3$$
$$(38)$$

Acknowledgement

The first author was supported by a National Aeronautics and Space Administration Cooperative Agreement NCC 5-82. The second Author is supported by the NASA Headquarters physical climate program, the NASA TRMM, and the interdisciplinary program of EOS. Each author thanks R. Adler and R. Kakar for their support. The views expressed herein are those of the authors and do not necessarily reflect the views of either agency.

6 References

Avissar, R., and F. Chen, 1993: Development and analysis of prognostic equations for mesoscale kinetic energy and mesoscale (subgrid-scale) fluxes for large scale atmospheric models. *J. Atmos. Sci.*, **50**, 3751–3774.

Avissar, R., and Y.-Q. Liu, 1996: Three-dimensional numerical study of shallow convective clouds and precipitation induced by land surface forcing. *J. Geophys. Res.*, **101 (D3)**, 7499–7518.

Balling, R.C., Jr., 1988: The climatic impact of a Sonoran vegetation discontinuity. *Climatic Change*, **13**, 99 – 109.

Caughey, S.J., and S.G. Palmer, 1979: Some aspects of turbulence structure through the depth of the convective boundary layer. *Quart. J. R. Met. Soc.*, **105**, 811-827.

Chen, F., and R. Avissar, 1994: Impact of land-surface moisture variability on local shallow convective cumulus and precipitation in large-scale models. *J. Appl. Meteor.*, **33**, 1382–1401.

Cutrim, E., D.W. Martin, and R. Rabin, 1995: Enhancement of cumulus clouds over deforested lands in Amazonia. *Bull. Amer. Meteor. Soc.*, **76**, 1801 – 1805.

Dalu, G.A., R.A. Pielke, R. Avissar, G. Kallos, M. Baldi, and A. Guerrini, 1991: Linear impact of thermal inhomogeneities on mesoscale atmospheric flow with zero synoptic wind. *Ann. Geophys.*, **9**, 641–647.

Deardorff, J. W., 1975: The development of boundary-layer turbulence models for use in studying the severe storm environment. *Proceedings of the SESAME Opening Meeting*, Boulder, NOTAA-ERL, 251-264.

Doran, J.C., S. Zhong, 1995: Variations in mixed-layer depths arising from inhomogeneous surface conditions. *J. Cli.*, **8**, 1965 - 1973.

Fankhauser, J.C., N.A. Crook, J. Tuttle, L.J. Miller, and C.G. Wade, 1995: Initiation of deep convection along boundary layer convergence lines in a semitropical environment. 1995: *Mon. Wea. Rev.*, **123**, 291 - 313.

Finkele, K., J.M. Hacker, H. Kraus, and R.A.D Byron-Scott, 1995: A complete sea-breeze circulation cell derived from aircraft observations. *Bound. Lay. Meterol.*, **73**, 299 - 317.

Frank, W.M. 1983: The cumulus parameterization problem. *Mon. Wea. Rev.*, **111**, 1859 - 1870.

Fritsch, J.M., and C.F. Chappell, 1980: Numerical Prediction of Convectively Driven Mesoscale Pressure Systems. Part I: Convective Parameterization. *J. Atmos. Sci.*, **37**, 1722-1741.

Hardy, K.R., and H. Otterstein, 1969: Radar investigations of convective patterns in the clear atmosphere. *J. Atmos. Sci.*, **26**, 666 - 672.

Houze Jr. R.A., 1989: Observed structure of mesoscale convective systems and implications for large-scale heating. *Q. J. R. Meteor. Soc.*, **115**, 425 - 461.

Kaimal, J.C, J.C. Wyngaard, D.A. Haugen, O.R. Coté, and Y. Izumi, 1976: Turbulence structure in the convective boundary layer. *J. Atmos. Sci.*, **33**, 2152 - 2169.

Kain, J.S. and J.M. Fritsch, 1990: A one dimensional entraining/detraining plume model and its application to convective parameterization. *J. Atmos. Sci.*, **47**, 2784-2802.

Kain, J.S., and J.M. Fritsch, 1992: The role of convective (trigger function) in numerical forecasts of mesoscale convective systems. *Meterol. Atmos. Phys.*, **49**, 93–106.

Klemp, J.B., and R. Wilhelmson, 1978: The simulation of three-dimensional convective storm dynamics. *J. Atmos. Sci.*, **35**, 1070 - 1096.

Konrad, T.G., 1970: The dynamics of the convective process in clear air as seen by radar. *J. Atmos. Sci.*, **27**, 1138 - 1147.

Lynn, B.H., D. Rind, R. Avissar, 1995a: The importance of mesoscale circulations generated by subgrid-scale landscape-heterogeneities in general circulation models. *J. Climate*, **8**, 191–205.

Lynn, B.H., F. Abramopoulos, and R. Avissar, 1995b: Using similarity theory to parameterize the mesoscale fluxes generated by landscape discontinuities in GCMs. *J. Climate*, **8**, 932–951.

Lynn, B.H., W.-K. Tao, P.J. Wetzel, 1998: A study of landscape generated deep moist convection. *Mon. Wea. Rev.*, **126**, 928 – 942.

Mahrt, L., 1987: Grid average surface fluxes. *Mon. Wea. Rev.*, **115**, 1550–1560.

Mahrt, L., J.S. Sun, D. Vickers, J.I. MacPherson, J.R. Pederson, and R.L.Desjardins, 1994: Observations of fluxes and inland breezes over a heterogeneous surface. *J. Atmos. Sci.*, 2484 – 2499.

Nicholls, M.E., R.A. Pielke, W.R. Cotton, 1991: A two-dimensional numerical investigation of the interaction between sea breezes and deep convection over the Florida pennisula. *Mon. Wea. Rev.*, **119**, 298 – 323.

Pielke, R.A., 1984: *Mesoscale Numerical Modelling*. Academic Press, New York, 612 pp.

Pielke, R.A., G.A. Dalu, J.S. Snook, T.J. Lee, and T.G.F. Kittel, 1991: Nonlinear influence of mesoscale land use on weather and climate. *J. Climate*, **4**, 1053–1069.

Pielke, R.A., T.J. Lee, J.H. Copeland, J.L. Eastman, C.L. Ziegler, and C.A. Finley, 1997: Use of USGS-provided data to improve weather and climate simulations. . *Ecol. Applic.*, **7**, 3 – 21.

Rogers, R.F., and J.M. Fritsch, 1996: A general framework for convective trigger functions. *Mon. Wea. Rev.*, **124**, 2438 –2452.

Rutlege, S.A., and P.V. Hobbs, 1984: The mesoscale and microscale structure and organization of clouds and precipitation in mid latitude clouds. Part XII: A diagnostic modeling study of precipitation development in narrow cold frontal rainbands. *J. Atmos. Sci.*, **41**, 2949 – 2972.

Segal, M., W. Schreiber, G. Kallos, R.A. Pielke, J.R. Garratt, J. Weaver, A. Rodi, and J. Wilson, 1989: The impact of crop areas in northeast Colorado on midsummer mesoscale thermal circlulations. *Mon. Wea. Rev.*, **117**, 809 – 825.

Smith, E.A., A.Y. Hsu, W.L. Crosson, R.T. Field, L.J. Fritschen, R.J. Gurney, E.T. Kanemasu, W.P. Kustas, D. Nie, W.J. Shuttleworth, J.B. Stewart, S.B. Verma, H.L. Weaver, and M.L. Wesley, 1992: Area-averaged surface fluxes and their time-space variability over the FIFE experimental domain. Paper Number 91JD03060. **J. Geoph. Res.**, **97**, 18599-18622.

Sellers, P., F. Hall, H. Margolis (and many others), 1995: The Boreal ecosystem – atmosphere study (BOREAS): An overview and early results from the 1994 field year.

Bull. Amer. Meteor. Soc. **75**. 1549 - 1577.

Soong. S.-T.. and Y. Ogura. 1980: Response of trade wind cumuli to large- scale processes. *J. Atmos. Sci.*. **37**. 2035–2050.

Sun. J. and L. Mahrt. 1994: Spatial distribution of surface fluxes estimated from remotely sensed data. *J. Appl. Meteorol.*. **33**. 1341 - 1353.

Stull. R.B.. 1988: *An Introduction to Boundary Layer Meteorology.* Kluwer. 666 pp.

Taconet. O. and A. Weill. 1983: Convective plumes in the atmospheric boundary layer as observed with an acoustic doppler radar. *Bound.- Layer Meteor.*. **25**. 143 - 158.

Tao. W.K.. and J. Simpson. 1993: Goddard Cumulus Ensemble Model. Part I: Model Description. *TAO*. **4**. 35–72.

Vidale. P.L.. R.A. Pielke. L.T. Steyaert. A. Barr. 1997: Case study modeling of turbulent and mesoscale fluxes over BOREAS region. *J. Geophy. Res.*. **102**. 29167 - 29188.

Walker. J.S. 1988: *Fourier Analysis.* Oxford University Press. New York. 440 pp.

Wang. J.. E.A.B. Eltahir. and R.L. Bras. 1998: Numerical simulation of nonlinear mesoscale circulations induced by the thermal heterogeneities of land surface. *J. Atmos. Sci.*. **55**. 447 - 464.

Wetzel. P.J. and A. Boone. 1995: A parameterization for Land-Atmosphere- Cloud Exchange (PLACE): Documentation and testing of a detailed process model of the partly cloudy boundary layer over heterogeneous land. *J. Climate*. **8**. 1810 - 1837.

Young. G.S.. 1987: Mixed layer spectra from aircraft measurements. *J. Atmos. Sci.*. **44**. 1251 - 1256.

Young. G.S.. 1988: Turbulence structure of the convective buondary layer. Part II: Phoenix 78 aircraft observations of thermals and their environment. *J. Atmos. Sci.*. p. 727 - 735.

Zeng. X. and R.A.Pielke. 1995: Landscape-induced atmospheric flow and its parameterization in large-scale numerical models. *J. Climate*. 1156 - 1177.

Zawadzki. I.I.. E. Torlaschi. and R. Sauvageau. 1981: The relationship between mesoscale thermodynamic variables and convective precipitation. *J. Atmos. Sci.*. **38**. 1535-1540.

List of Figures

Figure 10: Vertical profile of q_o obtained in Exp. 1w and 4w averaged over four hourly periods. These hourly periods are: (a) 10 – 11 LST. and (b) 11 – 12 LST. (c) 12 – 13 LST. and (d) 13 – 14 LST. The arrow indicates the approximate hieght of the cloud base.

Figure 11: Same as Fig. 12. but for the triggering variables on the upwind side and downwind of the dry patch in Exp. 8w.

Figure 12: Vertical profile of (a) heat and (b) moisture fluxes obtained in Exp. 3. The vertical convergence of these fluxes (not shown) contributes to the time rate of change of θ_o and q_o. The labels on the profiles in (a) correspond as follows: (1) $\overline{w'\theta'}^p$. (2) $\overline{w''\theta''}^p$. (3) $\overline{w'\theta''}^p$. (4) $\overline{w''\theta'}^p$. (5) $\langle w'\theta' \rangle$. and (6) $\langle w''\theta'' \rangle$. The labels on the profiles in (b) are as follows: (1) $\overline{w'q'}^p$. (2) $\overline{w''q''}^p$. (3) $\overline{w'q''}^p$. (4) $\overline{w''q'}^p$. (5) $\langle w'q' \rangle$. and (6) $\langle w''q'' \rangle$. The $\overline{o}^p$ indicates an average over the area of the parcel. Moist processes were turned off in this experiment.

Figure 13: Mesoscale (meso) and turbulent (turb) perturbations obtained in Exp. 3 for the triggering parcel on the downwind side of the dry patch. The data shown were the average of these perturbations obtained between 10 and 14 LST.

Figure 14: Same as Fig. 12. but for Exp. 8w. Moist processes were turned on in this experiment.

Figure 15: Power spectrum analysis of the u component obtained in experiments using the domains indicated (see Fig. 2). Simulations were produced using the observed sounding. with a light background wind (0.5 m s^{-1}). The data were averaged over 12 hours of simulation.

Figure 16: Vertical west-to-east cross section of mesoscale perturbation fields obtained at 13:00 LST in Exp. 3. Note. the derived mesoscale perturbations were independent of y. or the north-to-south direction. The dry patch was located from 32 to 96 km.

Fig. 17: Vertical profiles of the triggering variables obtained from model simulation results between 12 - 14 LST (left side) and 16 - 18 LST (right side) from experiments indicated by number on curve.

Fig. 18: Vertical profiles of the triggering variables obtained from the parameterization between 12 - 14 LST (left side) and 16 - 18 LST (right side) from experiments indicated by number on curve.

List of Tables

Table 7a: Constants required for the $\overline{w'^p}$.

Table 7b: Constants required for the $\overline{w''\theta'^p}$.

Table 7c: Constants required for the $\overline{w''q'^p}$.

Table 8: Miscellaneous Definitions of Variables (H is the planetary boundary layer height).

Table 1: Model input parameters used for numerical simulations (Numbers in parentheses refer to simulations with moist processes "turned on."

Condition	*Value*
Day of the Year	July 27
Latitude	28°
Initialization time	6 a.m.
Integration time step	5 s
Simulation length	12 hr
Height of the atmosphere	10 km (20 km)
Number of vertical grid elements	30 (50)
Vertical Grid Resolution (Stretched)	20 - 500 m
Lateral Boundary Conditions	Periodic
Horizontal Grid Resolution (Fixed)	250×250 m^2

Table 2: Land characteristics used for the numerical simulations.

Land Characteristic	*Value*
Surface Roughness (m)	1.11
Surface Albedo	0.20
Surface Emissivity	1.00
Soil Texture	sandy-clay-loam
Soil Depth (m)	10
Root Zone Depth (m)	1.60
Porosity (mm^3 mm^{-1})	0.404
Field Capacity (mm^3 mm^{-3})	0.298
Wilting Point (mm^3 mm^{-3})	0.137
Slope of Retention Curve	6.77
Saturated Matric Potential (cm)	-13.49
Saturated Hydraulic Conductivity (cm $^{-1}$)	4.45×10^{-4}
Vegetation	Tall. Broadleaf and Needleleaf Trees
Leaf Area Index	2.46
Minimum Stomatal Resistance (s/m)	1.00
Maximum Stomatal Resistance (s/m)	10.0
Plant Critical Water Potential (m)	-200

Table 3a: Description of model experiments with moist processes turned on. The v component of the wind was set equal to 0.

Name	*Patch Sizes (L, km)*	*Special Condition*
Exp. 1w	64 (Domain 1)	Background u wind a constant, 0.5 m s^{-1}
Exp. 2w	40, 32	Background u wind a constant, 0.5 m s^{-1}
Exp. 3w	16, 24, 24.5 (Domain 2)	Background u wind a constant, 0.5 m s^{-1}
Exp. 4w	7.5, 4, 16, 4, 8, 20, 4 (Domain 3)	Background u wind a constant, 0.5 m s^{-1}
Exp. 5w	$3 < L < 8$	Background u wind a constant, 0.5 m s^{-1}
Exp. 6w	$2 < L < 6$	Background u wind a constant, 0.5 m s^{-1}
Exp. 7w	$0.25 < L < 1$ (Domain 4)	Background u wind a constant, 0.5 m s^{-1}
Exp. 8w	64	Observed u background wind
Exp. 9w	16, 24, 24.5	Observed u background wind
Exp. 10w	40, 32	Observed u background wind
Exp. 11w	7.5, 4, 16, 4, 8, 20, 4	Observed u background wind

Table 3b: Description of model experiments with moist processes turned off. The v component of the wind was set equal to 0.

Name	*Patch Sizes (L, km)*	*Special Condition*
Exp. 1	64 (Domain 1)	Background u wind 0.5 m s^{-1}
Exp. 2	7.5,4, 16, 4, 8, 20 (Domain 3)	Background u wind 0.5 m s^{-1}
Exp. 3	64	Observed (u) background wind
Exp. 4	7.5,4, 16, 4, 8, 20	Observed (u) background wind
Exp. 5	64	$\theta_{sl} = 0.177$ (dry patches), $\theta_s l = 0.257$ (wet patches) Background u wind 0.5 m s^{-1}
Exp. 6	64	Increased stability by 3.5 K 1000 m^{-1} Background u wind 0.5 m s^{-1}
Exp. 7	64	Decreased $\hat{q}$ to 50% of observed Background u wind 0.5 m s^{-1}
Exp. 8	64	10° latitude Background u wind 0.5 m s^{-1}
Exp. 9	64	50° latitude Background u wind 0.5 m s^{-1}
Exp. 10	64	Observed (u) equals one-half background wind
Exp. 11	64	Observed (u) equals twice background wind
Exp. 12	16, 24, 24.5 (Domain 2)	Background u wind a constant, 0.5 m s^{-1}
Exp. 13	$0.25 < L < 1$ (Domain 4)	Background u wind a constant, 0.5 m s^{-1}

Table 4: Rainfall versus average patch size and largest patch size. Exps. 1w – Exp. 7w were each produced using a light background wind. Exps. 8w – 11w were produced using the observed (west-to-east) background wind. The correlation coefficient for average patch size versus rainfall for Exps. 1w – Exp. 7w was 0.32, while the correlation coefficient between the biggest patch size and rainfall was 0.45. For Exps. 8w – 11w, . the correlation coefficient between the average patch size and rainfall was 0.77, while the correlation coefficient between the biggest patch size and rainfall was 0.79 (in these two sets, the range of the rainfall was relatively small).

Name	*Average Patch Size (km)*	*Biggest Patch Size*	*Accumulated Rainfall (mm)*
Exp. 1w	64	64	1.35
Exp. 2w	36	40	1.28
Exp. 3w	21.5	24.5	1.31
Exp. 4w	9	20	1.48
Exp. 5w	≈ 4.5	≈ 10	1.33
Exp. 6w	≈ 3.0	≈ 6	1.23
Exp. 7w	≈ 0.5	≈ 1.0	0.98
Exp. 8w	64	64	1.18
Exp. 9w	36	40	1.13
Exp. 10w	21.5	24.5	1.14
Exp. 11w	9	20	1.14

Table 5: Budget equations terms. An X in the appropriate column indicates that the corresonding term needs to be included in its particular budget equation. A $\surd$ indicates that an appropriate parameterization needs to be developed for that term; otherwise, parameterizations exist for that term in the literature. The $\overline{\phi}^p$ indicates an average over the area of the triggering parcel. $\phi_o = \overline{\phi'}^p + \overline{\phi''}^p$. The variable ϕ' represents the mesoscale field obtained after a filtering of the high resolution data. The variable ϕ'' represents the large eddy turbulent field obtained as the residual of the filtered and original fields.

Term	*Include*	*Develop Parameterization*
$\langle w'\theta'\rangle$		
$\langle w''\theta''\rangle$	X	
$\langle w'''\theta'''\rangle$	X	
$\overline{w'\theta'}^p$		
$\overline{w''\theta''}^p$	X	
$\overline{w''\theta'}^p$	X	$\surd$
$\overline{w'\theta''}^p$		
$\overline{w'''\theta'''}^p$	X	
$\langle w'q'\rangle$		
$\langle w''q''\rangle$	X	
$\langle w'''q'''\rangle$	X	
$\overline{w'q'}^p$		
$\overline{w''q''}^p$	X	
$\overline{w''q'}^p$	X	$\surd$
$\overline{w'q''}^p$		
$\overline{w'''q'''}^p$	X	

Table 6: Variables required for Parameterization.

Variable	*Description*	*Units*
L	Length Scale of Patch	m
R_o	Local Radius of Deformation	km
H	Planetary Boundary Layer Height (for each dry patch)	m
$\Delta w'''\theta'''$	Gradient of Surface Sensible Heat Fluxes	K m s^{-1}
Θ	Grid-Scale (Mean) Planetary Boundary Layer Temperature	K
Q	Grid-Scale Specific Humidity	
U	Background Wind	m s^{-1}
U_o^u	A function of patch size for parcels on upwind side of dry patch	m s^{-1}
U_o^d	For parcels on upwind side of dry patch	m s^{-1}
tau	time	s

Table 7a: Constants required for the $\overline{w'^p}$.

Variable	*Value*
α_1	80.3
α_2	-76.6
$alpha_3$	-73.0
α_4	75.8
α_5	20.2

Table 7b: Constants required for the $\overline{w''\theta'^p}$.

Variable	*Value*	*Units*
α_1	0.55	
α_2	-0.41	
$alpha_3$	0.20	
α_4	0.53	
α_5	-0.42	

Table 7c: Constants required for the $\overline{w''q'^p}$.

Variable	*Value*	*Units*
α_1	32.1	
α_2	20.8	
$alpha_3$	-31.1	
α_4	-26.5	
α_5	21.9	

Table 8: Miscellaneous Definitions of Variables (H is the planetary boundary layer height).

Variable	*Definition*
$\tilde{\phi}$	Grid-scale average over domain of regional model
ϕ'	Mesoscale perturbation (horizontal-scale > than $3H$)
ϕ''	Large eddy perturbation (50 m < horizontal-scale $\leq 3H$)
ϕ'''	Small eddy perturbation (horizontal-scale $\leq$ 50 m)
ϕ_s	Subgrid-scale perturbations obtained with GCE
ϕ_o	Parcel value of ϕ; ϕ_s averaged over square area of parcel
$\overline{\phi}^p$	Average of ϕ over square area of parcel

1a

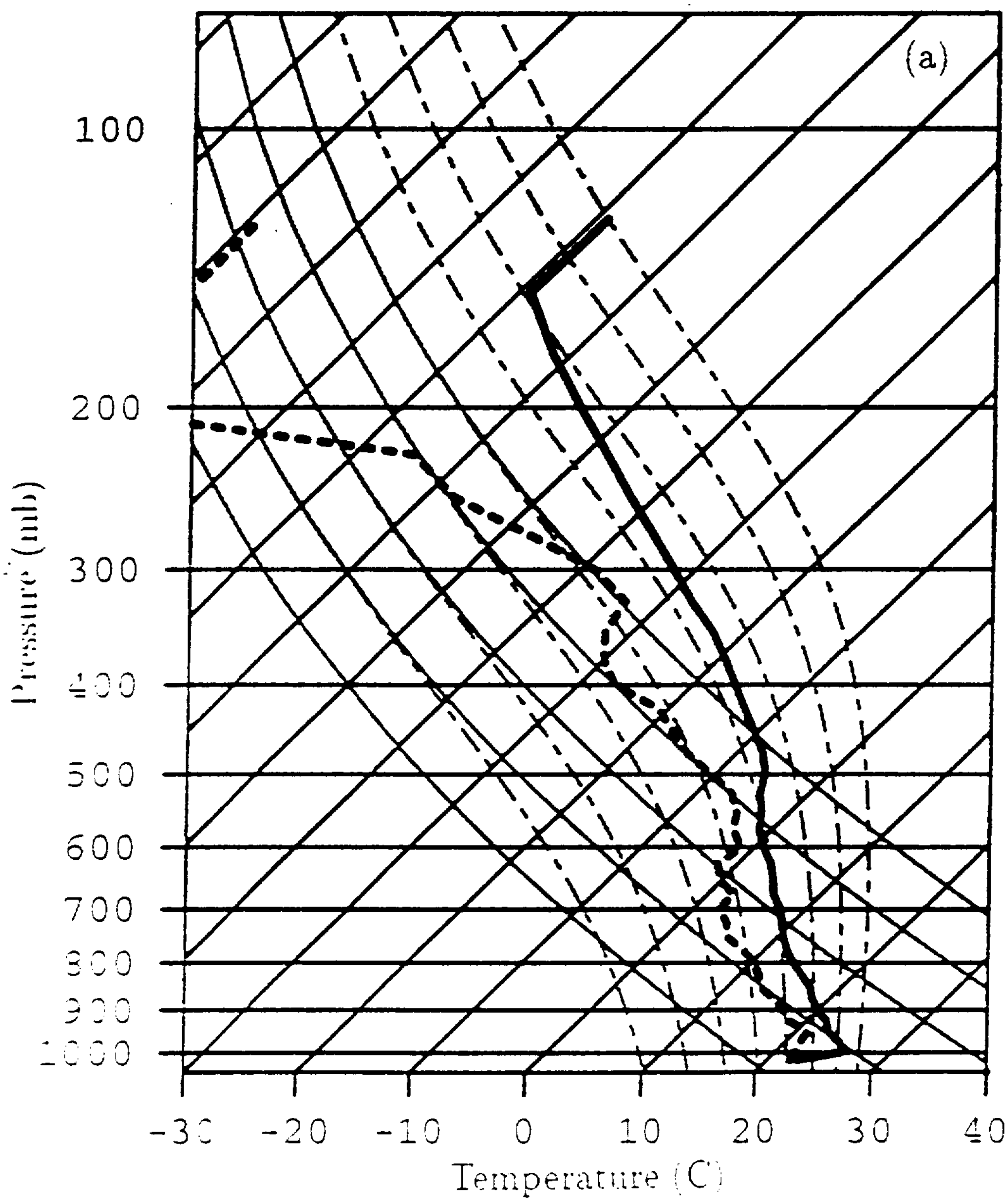
(a)
100
200
300
400
500
600
700
800
900
1000
Pressure (mb)
-30
-20
-10
0
10
20
30
40
Temperature (C)

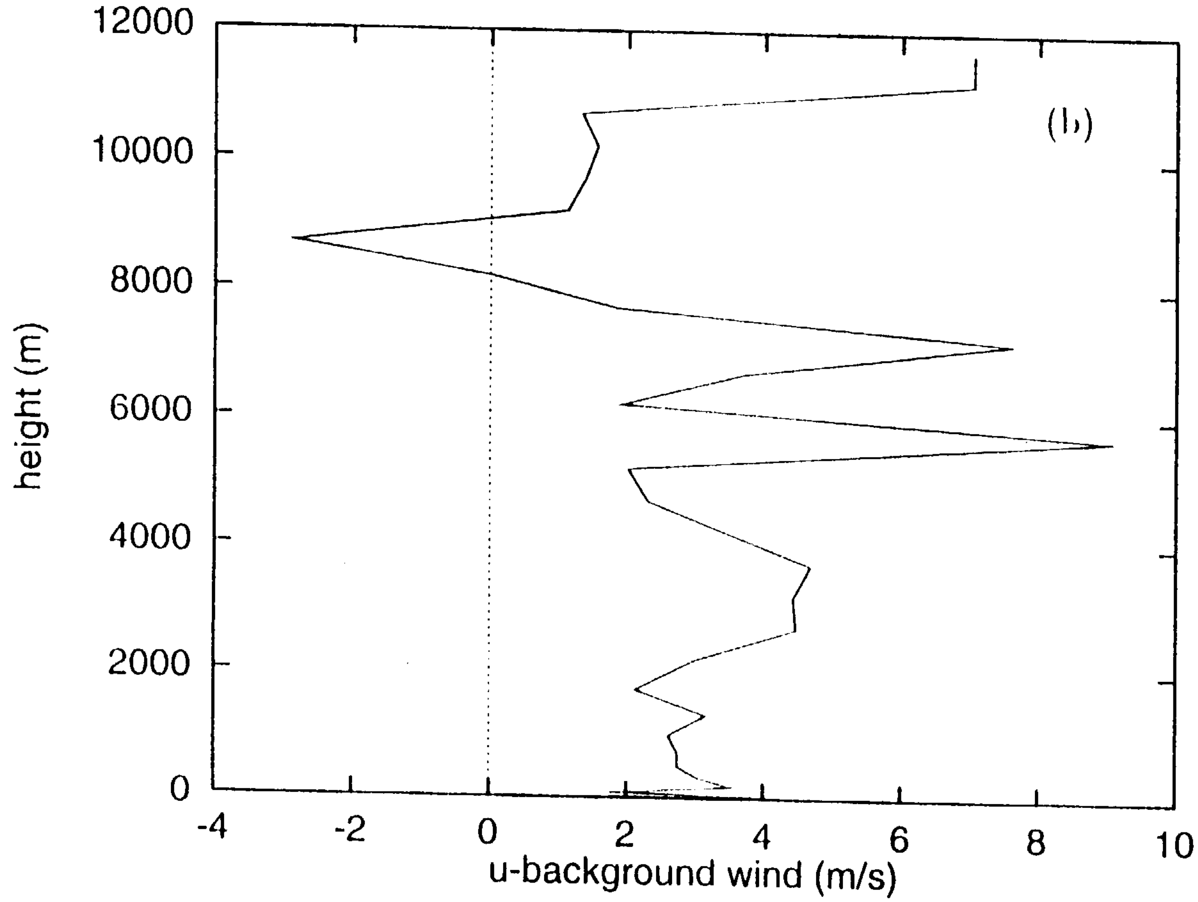

12000
10000
8000
6000
4000
2000
0
height (m)
-4
-2
0
2
4
6
8
10
u-background wind (m/s)
(b)

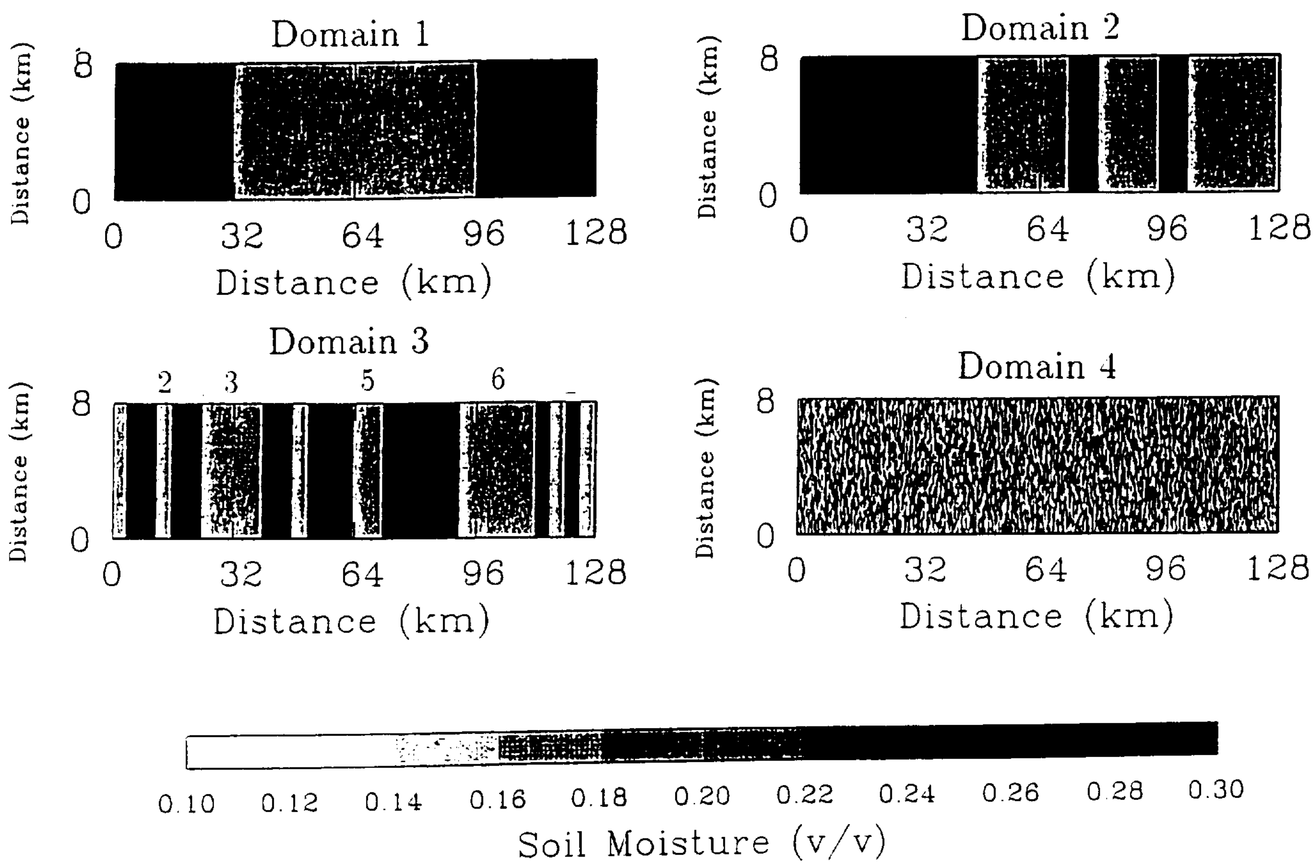

Domain 1
Domain 2
Domain 3
Domain 4
2
3
5
6
Distance (km)
8
0
0
32
64
96
128
Distance (km)
0.10
0.12
0.14
0.16
0.18
0.20
0.22
0.24
0.26
0.28
0.30
Soil Moisture (v/v)

3

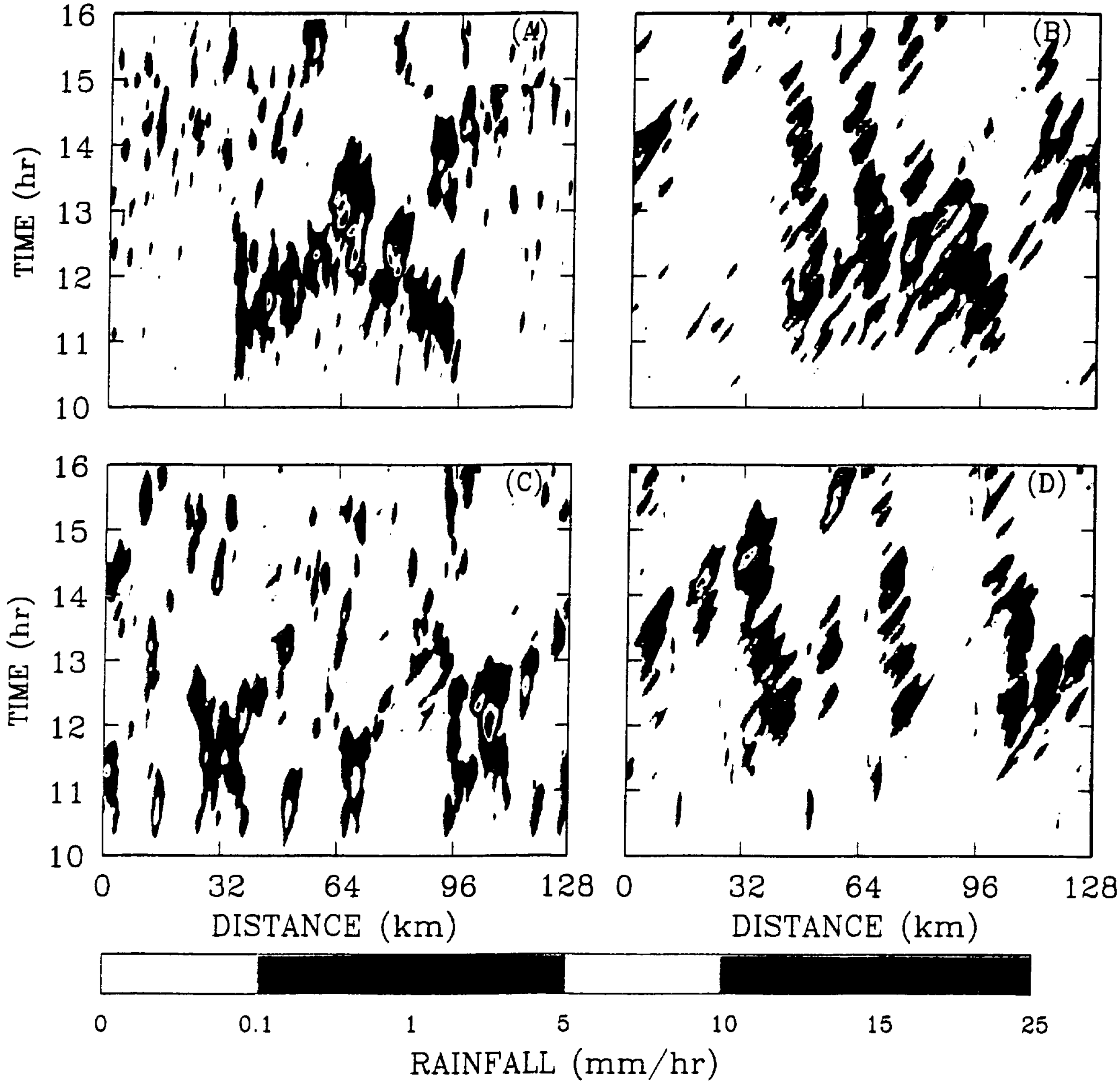
(A)
(B)
(C)
(D)
TIME (hr)
10
11
12
13
14
15
16
0
32
64
96
128
DISTANCE (km)
0
0.1
1
5
10
15
25
RAINFALL (mm/hr)

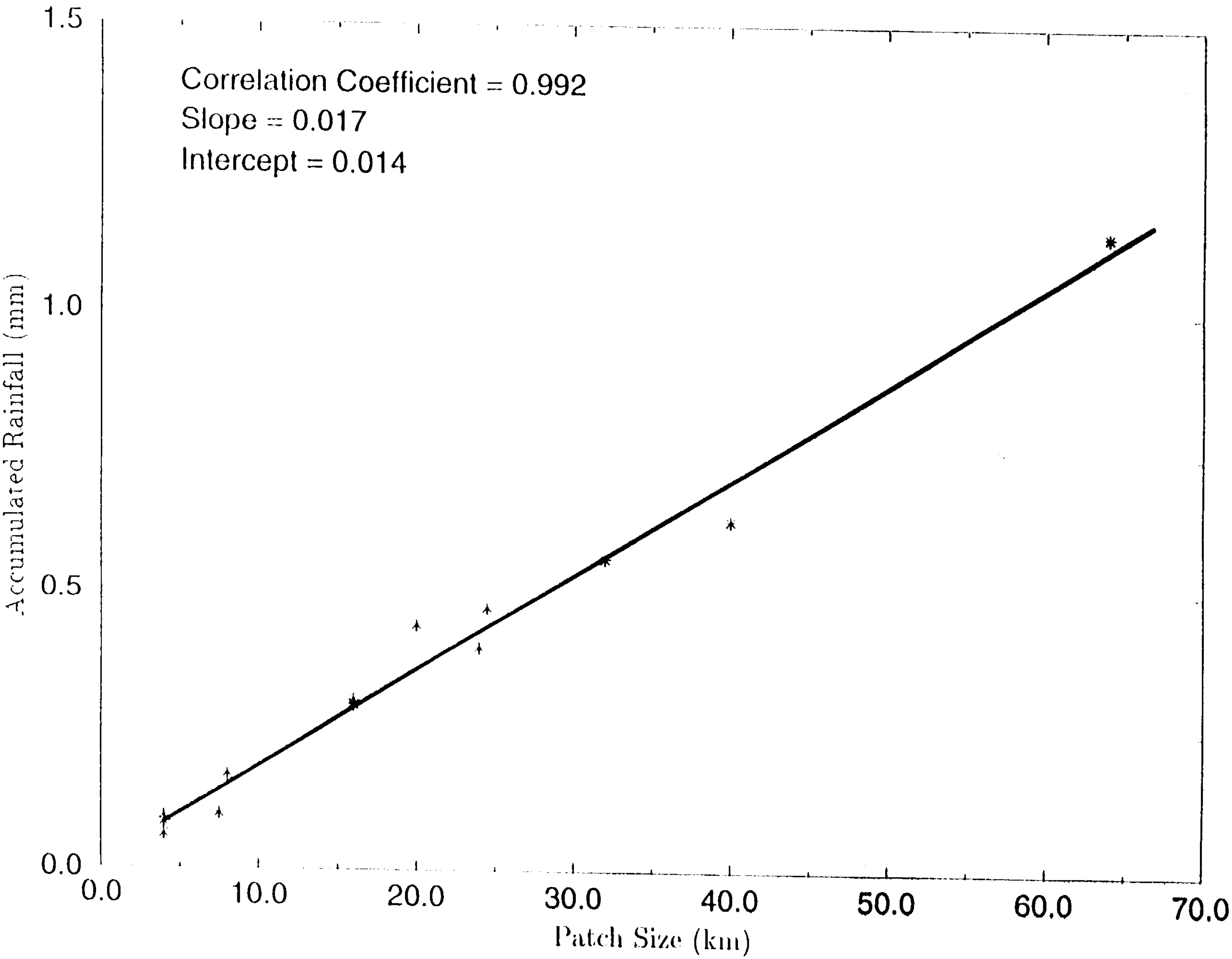

Correlation Coefficient = 0.992
Slope = 0.017
Intercept = 0.014
Accumulated Rainfall (mm)
Patch Size (km)
0.0
0.5
1.0
1.5
0.0
10.0
20.0
30.0
40.0
50.0
60.0
70.0

4

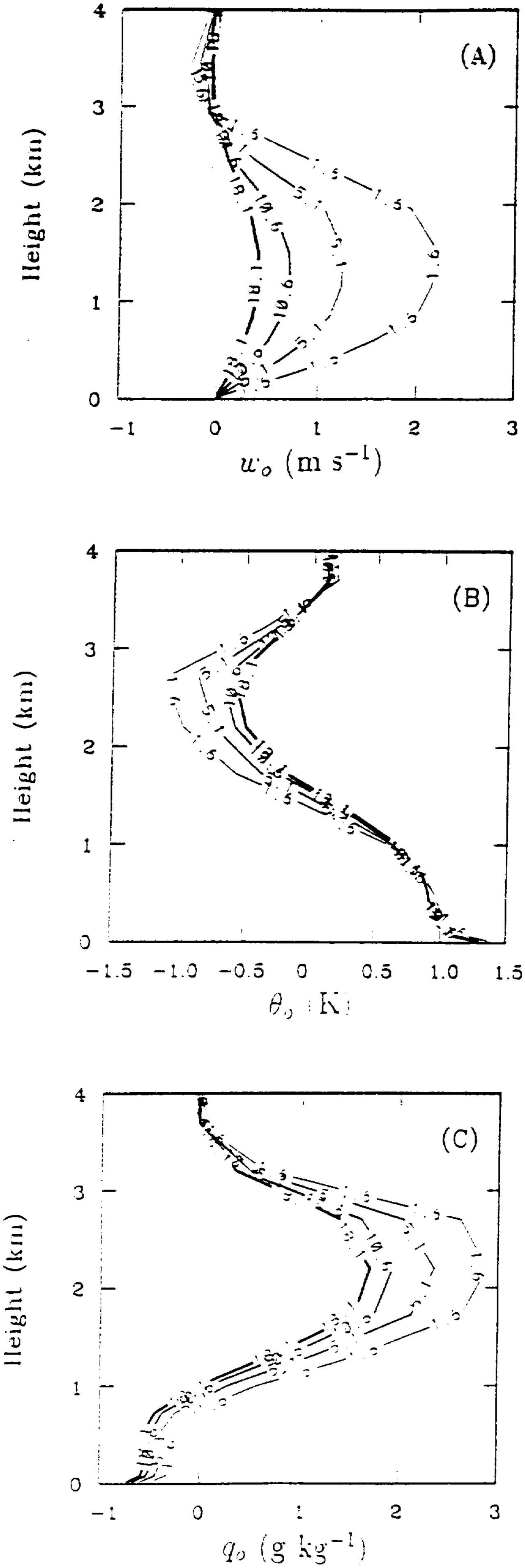
(A)
Height (km)
u_o (m s^{-1})
(B)
Height (km)
θ_o (K)
(C)
Height (km)
q_o (g kg^{-1})

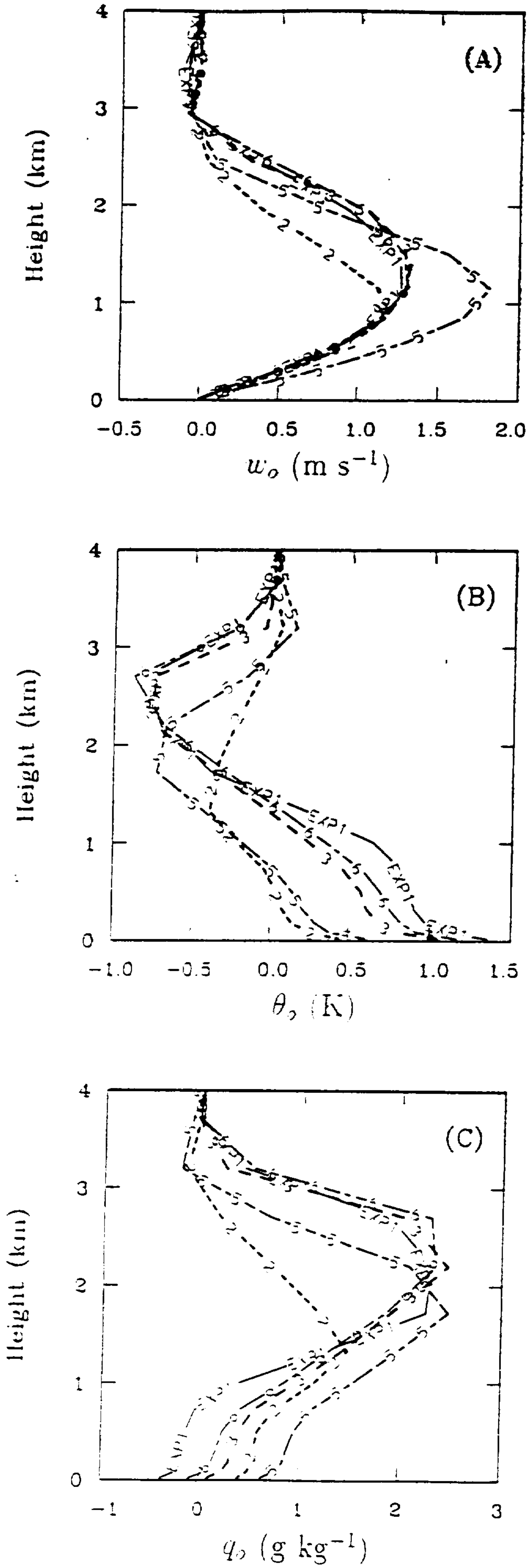
(A)
Height (km)
w_o (m s^{-1})
(B)
Height (km)
θ_2 (K)
(C)
Height (km)
q_2 (g kg^{-1})

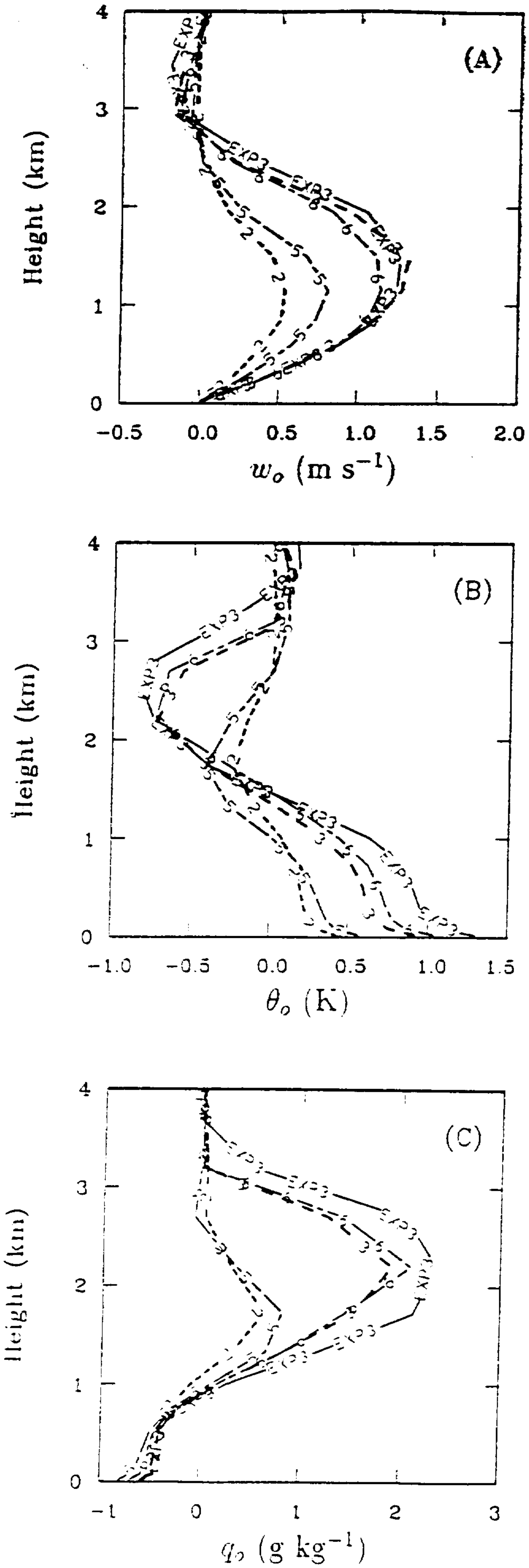

(A)
Height (km)
w_o (m s^{-1})
EXP3
6
5
2
(B)
Height (km)
θ_o (K)
EXP3
6
5
2
(C)
Height (km)
q_o (g kg^{-1})
EXP3
6
5
2

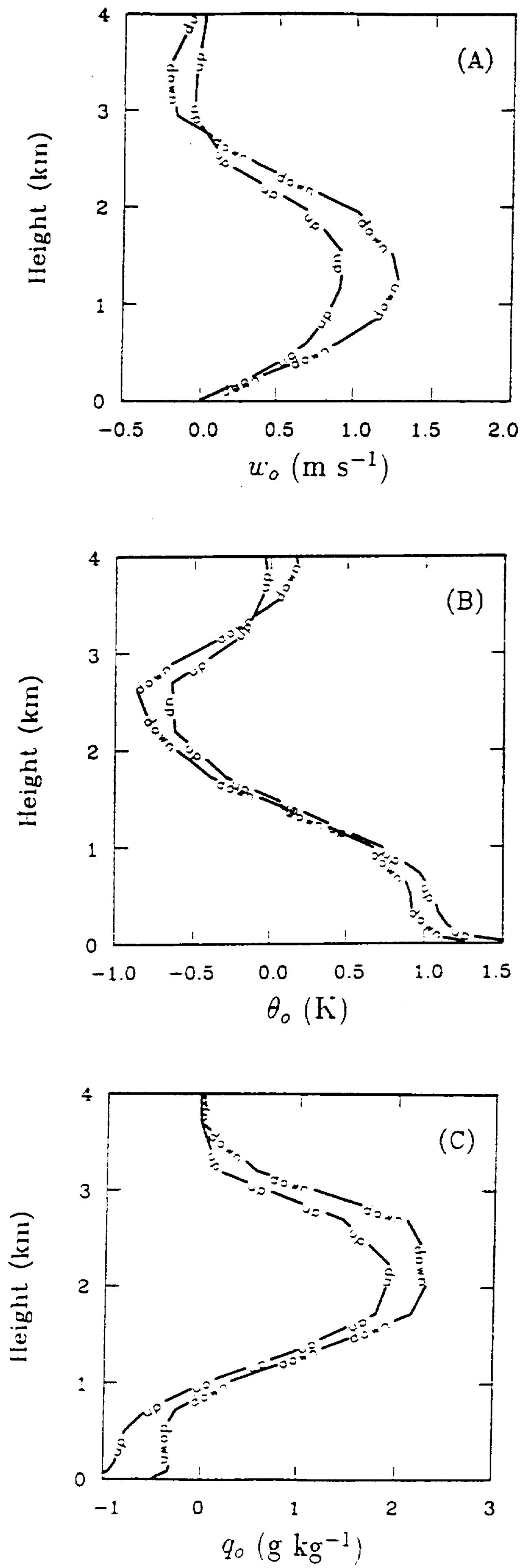
(A)
Height (km)
u_o (m s^{-1})
−0.5 0.0 0.5 1.0 1.5 2.0
up
down
(B)
Height (km)
θ_o (K)
−1.0 −0.5 0.0 0.5 1.0 1.5
(C)
Height (km)
q_o (g kg^{-1})
−1 0 1 2 3
0 1 2 3 4

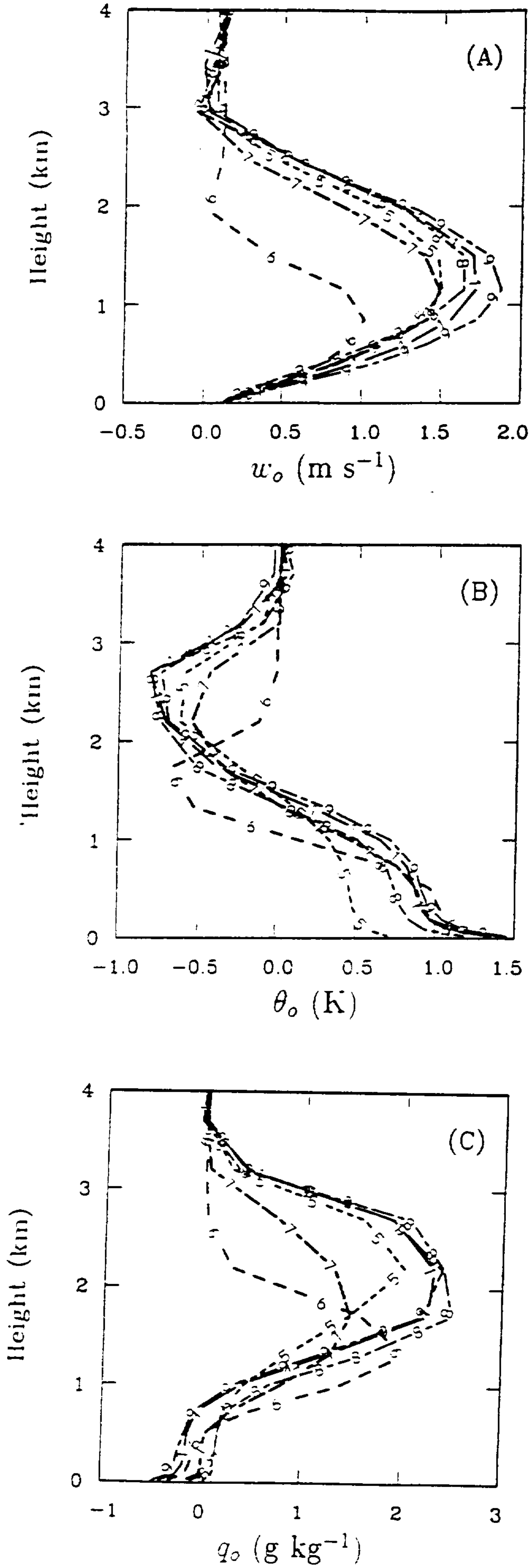
(A)
Height (km)
w_o (m s^{-1})
(B)
Height (km)
θ_o (K)
(C)
Height (km)
q_o (g kg^{-1})

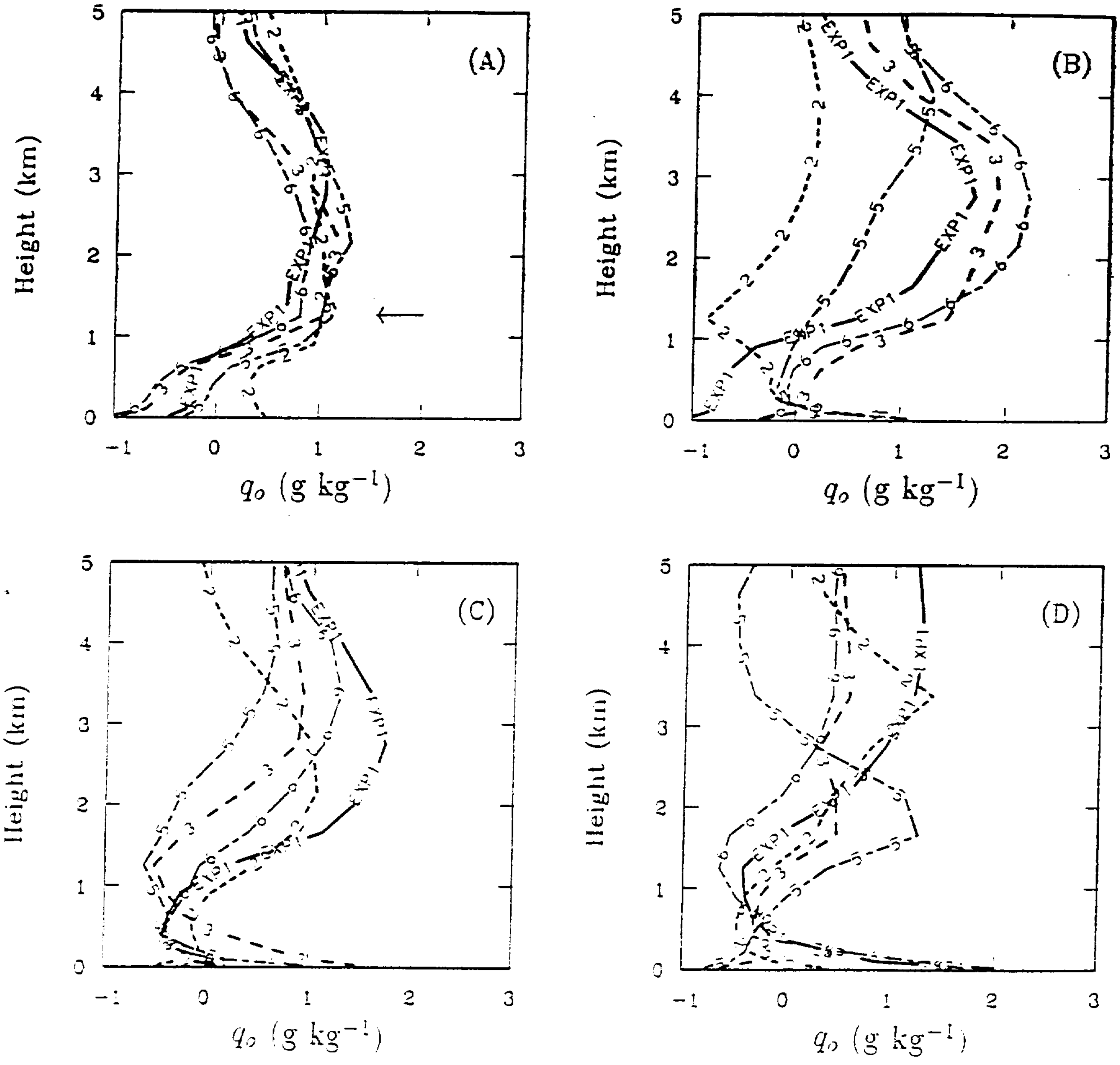
(A)
(B)
(C)
(D)
Height (km)
q_o (g kg^{-1})
EXP1

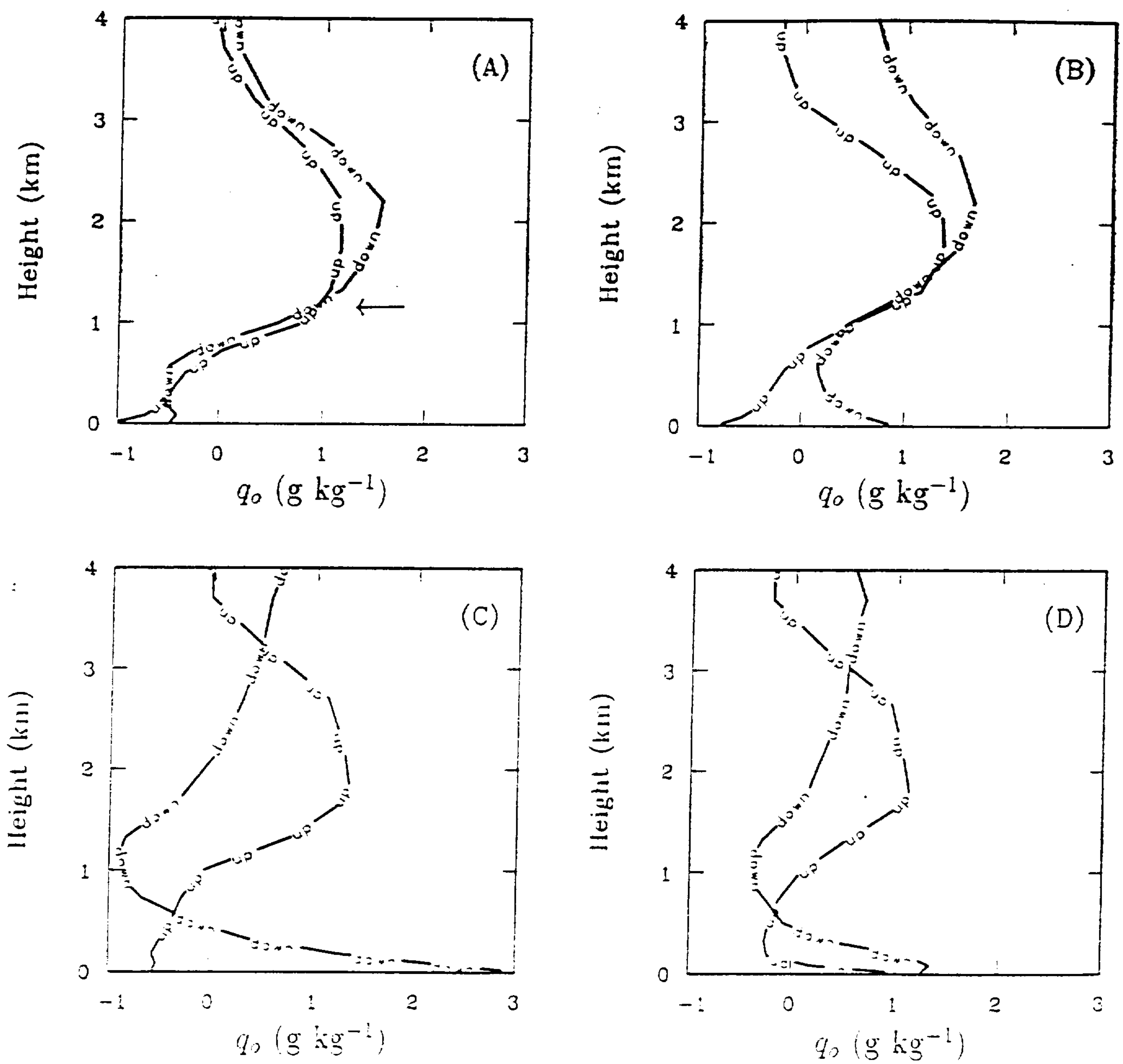
(A)
(B)
(C)
(D)
Height (km)
q_o (g kg^{-1})
up
down

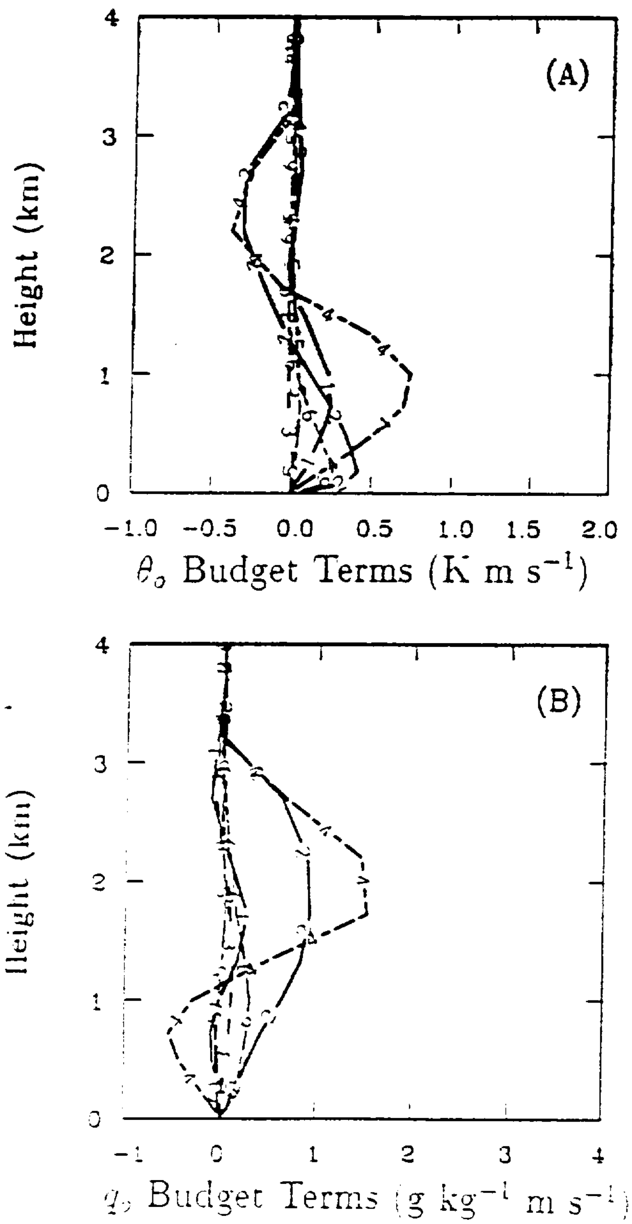
(A)
Height (km)
4
3
2
1
0
−1.0
−0.5
0.0
0.5
1.0
1.5
2.0
θo Budget Terms (K m s−1)
(B)
Height (km)
4
3
2
1
0
−1
0
1
2
3
4
qo Budget Terms (g kg−1 m s−1)

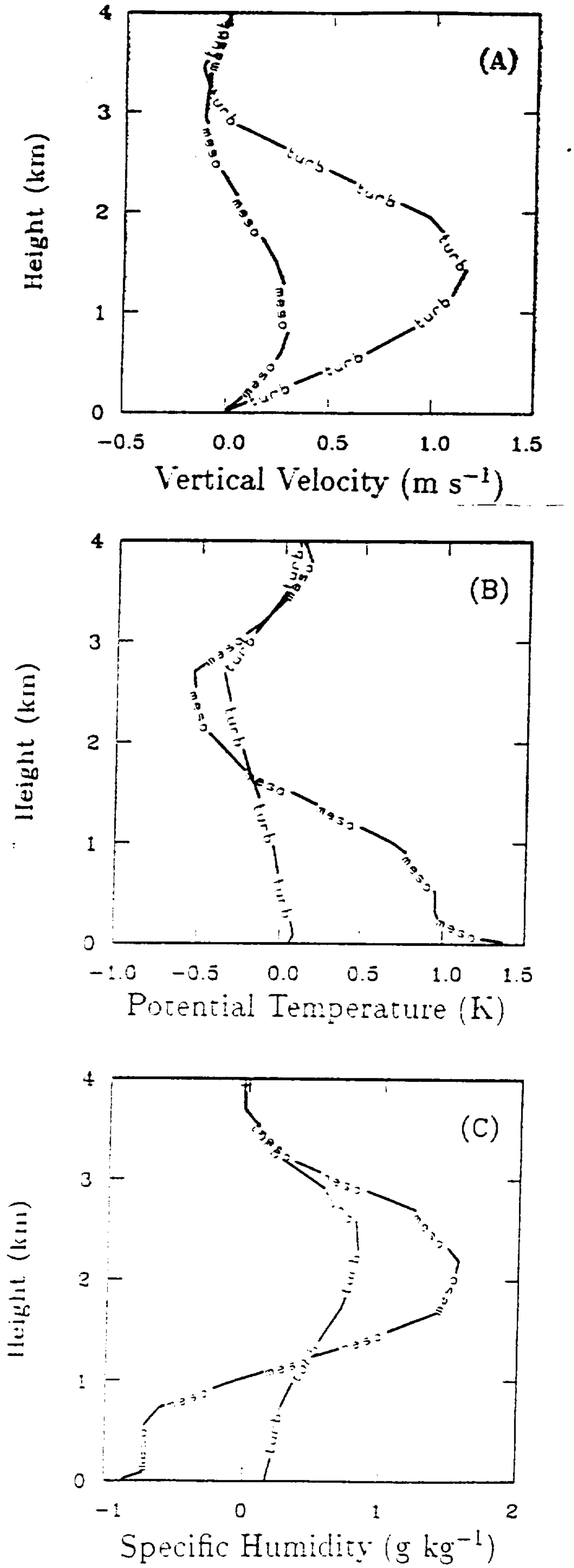
(A)
Height (km)
Vertical Velocity (m s^{-1})
turb
meso
(B)
Height (km)
Potential Temperature (K)
turb
meso
(C)
Height (km)
Specific Humidity (g kg^{-1})
turb
meso

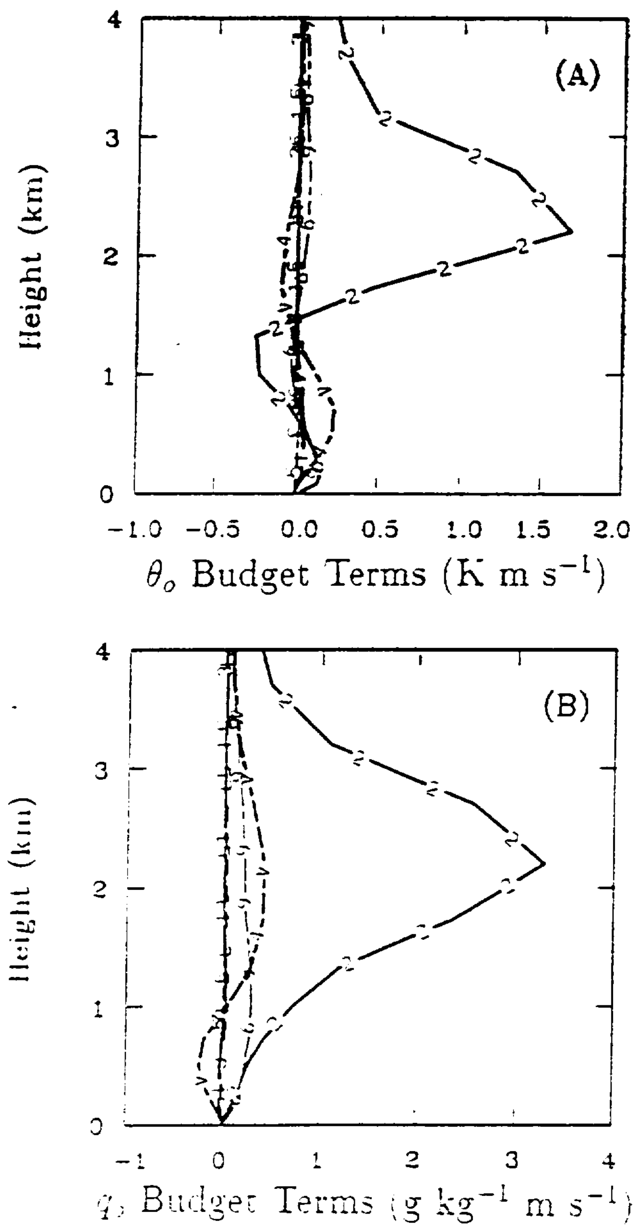

(A)
Height (km)
4
3
2
1
0
−1.0 −0.5 0.0 0.5 1.0 1.5 2.0
θ_o Budget Terms (K m s^{-1})
(B)
Height (km)
4
3
2
1
0
−1 0 1 2 3 4
q_o Budget Terms (g kg^{-1} m s^{-1})

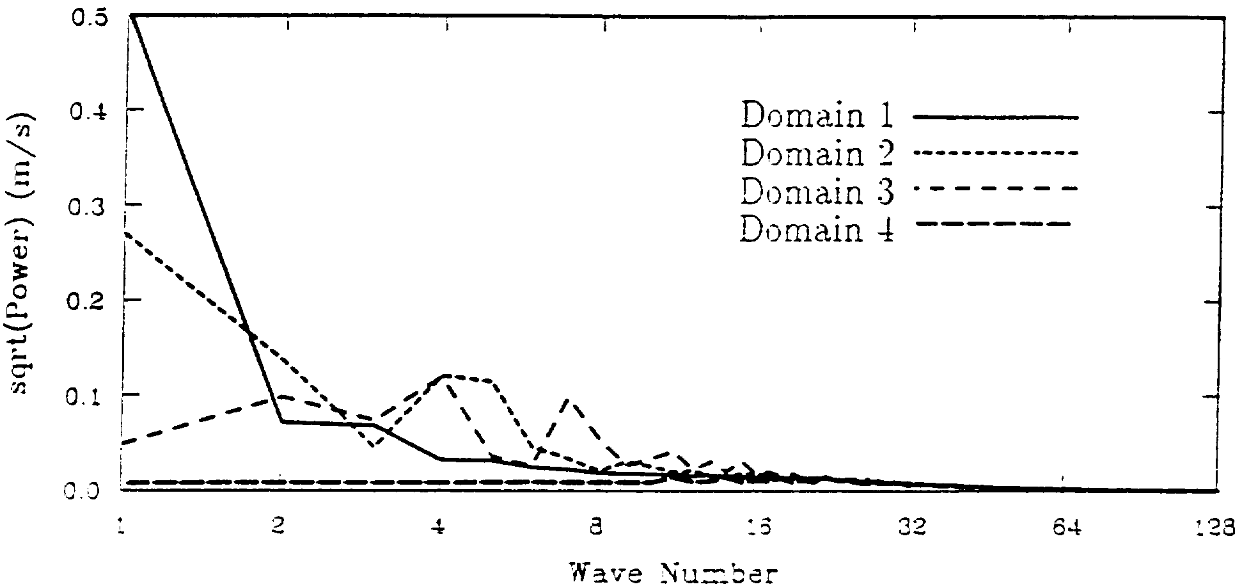
Domain 1
Domain 2
Domain 3
Domain 4
sqrt(Power) (m/s)
0.5
0.4
0.3
0.2
0.1
0.0
1
2
4
8
16
32
64
128
Wave Number

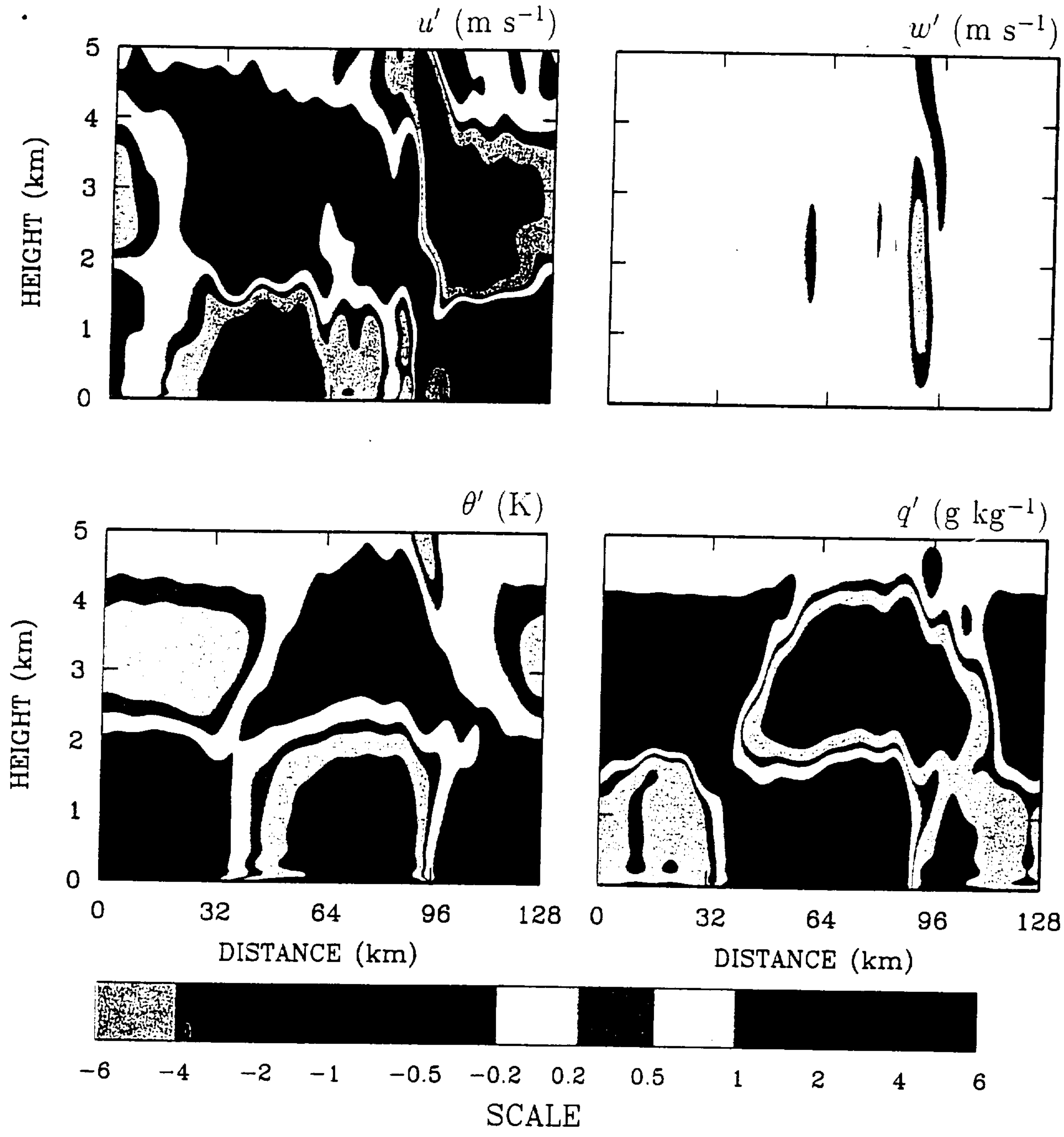

u' (m s⁻¹)
w' (m s⁻¹)
θ' (K)
q' (g kg⁻¹)
HEIGHT (km)
0 1 2 3 4 5
DISTANCE (km)
0 32 64 96 128
−6 −4 −2 −1 −0.5 −0.2 0.2 0.5 1 2 4 6
SCALE

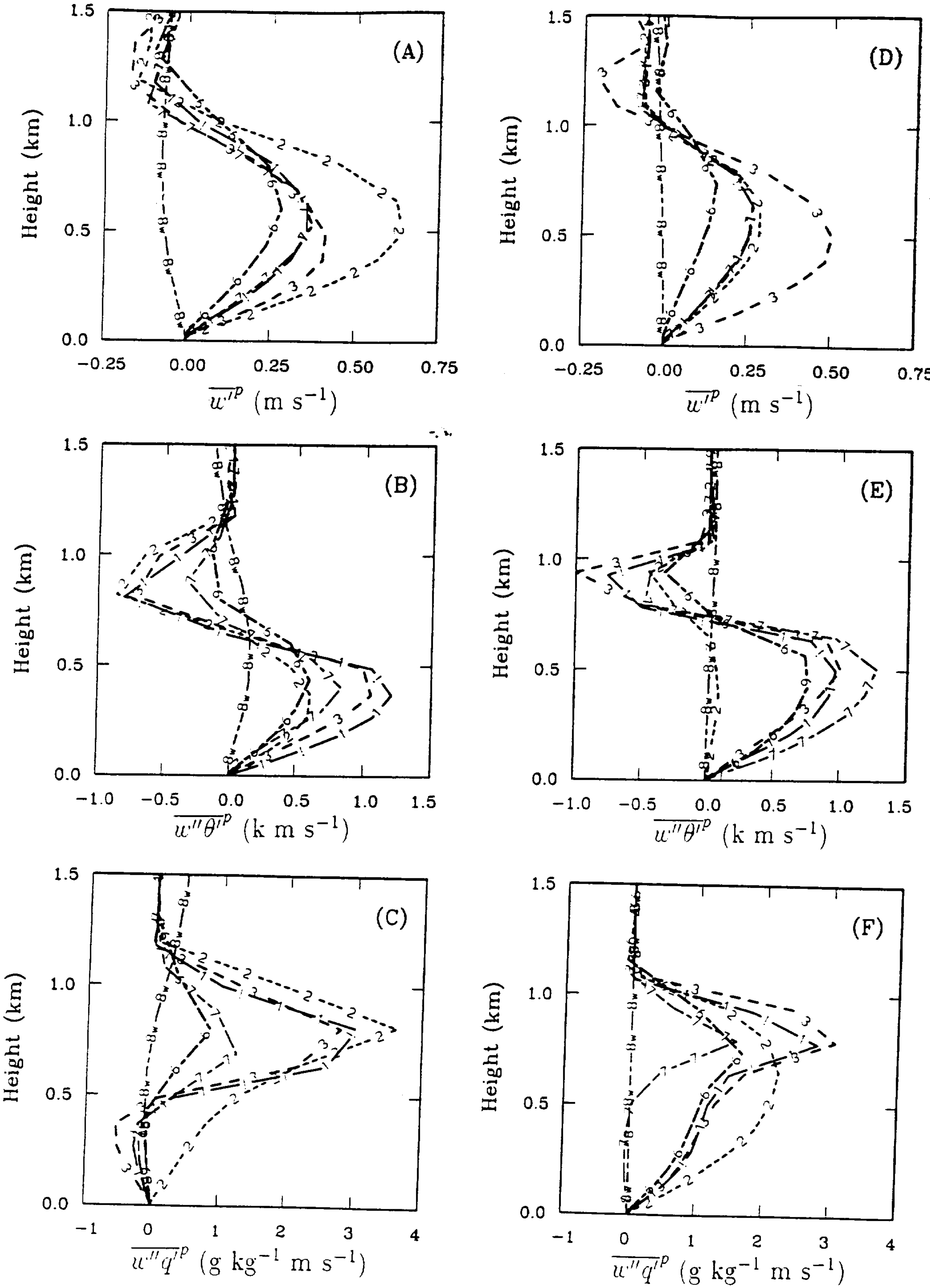
(A)
(B)
(C)
(D)
(E)
(F)
Height (km)
$\overline{w'^p}$ (m s^{-1})
$\overline{w''\theta'^p}$ (k m s^{-1})
$\overline{w''q'^p}$ (g kg^{-1} m s^{-1})

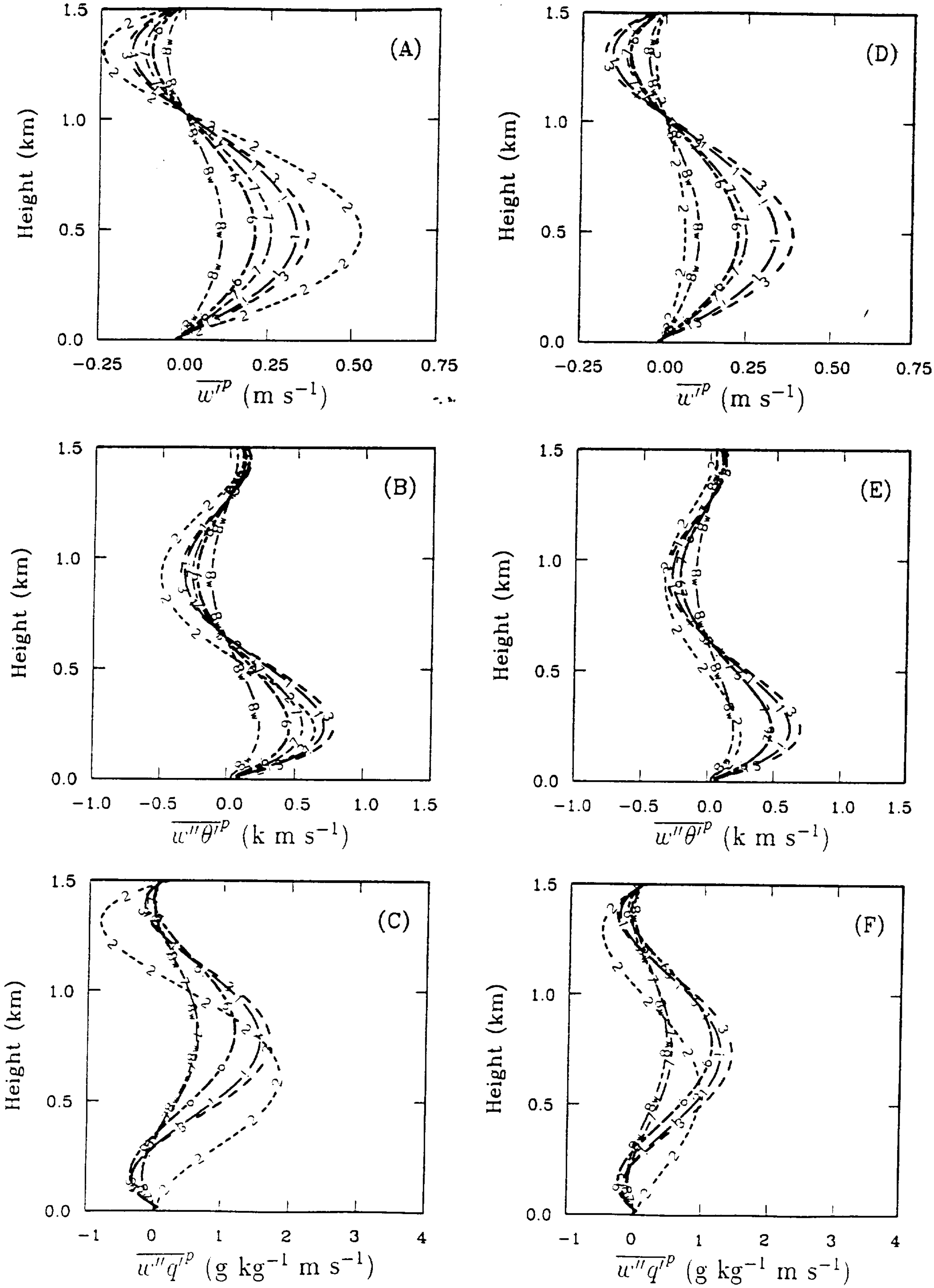
(A)
(B)
(C)
(D)
(E)
(F)
Height (km)
$\overline{w'^p}$ (m s^{-1})
$\overline{w''\theta'^p}$ (k m s^{-1})
$\overline{w''q'^p}$ (g kg^{-1} m s^{-1})